Deep Intermediate-Band Surface Photometry of NGC 5907

Zhongyuan Zheng[1,3], Zhaohui Shang[1,2,3], Hongjun Su[1], David Burstein[5], Jiansheng Chen[1,3], Zugan Deng[6,3], Yong-Ik Byun[4,9], Rui Chen[1,3], Wen-ping Chen[4], Licai Deng[1,3], Xiaohui Fan[1,7], Li Zhi Fang[10] Jeff J. Hester[5], Zhaoji Jiang[1,3], Yong Li[5], Weipeng Lin[1,3], Wei-hsin Sun[4], Wean-shun Tsay[4], Rogier A. Windhorst[5], Hong Wu[1,3], Xiaoyang Xia[8,3], Wen Xu[1,5], Suijian Xue[1,3], Haojing Yan[1,5], Zheng Zheng[1,3], Xu Zhou[1,3], Jin Zhu[1,3] and Zhenglong Zou[1,3]

Received _____; accepted _____

[1]Beijing Astronomical Observatory, Chinese Academy of Sciences, Beijing 100080, P. R. China

[2]Department of Astronomy, University of Texas at Austin, Austin, TX 78712

[3]Chinese Academy of Sciences–Peking University joint Beijing Astrophysics Center, Beijing, 100871, P. R. China

[4]Institute of Astronomy, National Central University, Chung-Li, Taiwan

[5]Department of Physics and Astronomy, Box 871504, Arizona State University, Tempe, AZ 85287–1504

[6]Graduate School, Chinese Academy of Sciences, Beijing 100080, P. R. China

[7]Princeton University Observatory, Princeton, New Jersey, 08544

[8]Department of Physics, Tianjin Normal University, P. R. China

[9]Center for Space Astrophysics and Department of Astronomy, Yonsei University, Seoul, 120–749, Korea

[10]Department of Physics, University of Arizona, Tucson, Arizona, 85721

ABSTRACT

Intrigued by the initial report of an extended lumiosity distribution perpendicular to the disk of the edge-on Sc galaxy NGC 5907, we have obtained very deep exposures of this galaxy with a Schmidt telescope, large-format CCD, and intermediate-band filters centered at 6660Å and 8020Å. These two filters, part of a 15-filter set, are custom-designed to avoid the brightest (and most variable) night sky lines. As a result, our images are able to go deeper, with lower sky noise than those taken with broad-band filters at similar effective wavelengths: e.g., 0.6 e^- arcsec^{-2} sec^{-1} for our observations vs. 7.4 e^- arcsec^{-2} sec^{-1} for the R-band measures of Morrison et al. In our assessment of both random and systematic errors, we show that the flux level where the errors of observation reach 1 mag arcsec^{-2} are 29.00 mag arcsec^{-2} in the 6660Å image (corresponding to 28.7 in R-band) and 27.4 mag arcsec^{-2} in the 8020Å image (essentially on the I-band system).

As detailed in Shang et al., our observations show NGC 5907 has a luminous ring around it that most plausibly is due to the tidal disruption of a dwarf spheroidal galaxy by the much more massive spiral. Here we show that, fainter than 27th R mag arcsec^{-2}, the surface brightness around NGC 5907 is strongly asymmetric, being mostly brighter on NW (ring) side of the galaxy midplane. This asymmetry rules out a halo for the origin of the faint surface brightness we see. We find this asymmetry is likely an artifact owing to a combination of ring light and residual surface brightness at faint levels from stars that our star-masking procedure cannot completely eliminate. The possible existence of an optical face-on warp in NGC 5907, suggested by our VLA HI observations, is too confused with foreground star contamination to be independently studied.

Good agreement with the surface photometry of NGC 5907 by Morrison et al. and other workers lead us to conclude that their data are similarly affected at faint levels by ring light and residual effects from their star masking procedures. Inspection of the images published by Morrison et al. and Sackett et al. confirm this to be the case. Thus, we conclude that NGC 5907 does not have a faint, extended halo.

Subject headings: galaxies: individual (NGC 5907) – galaxies: interactions – galaxies: spiral – galaxies: photometry

1. INTRODUCTION

Until Sackett et al. (1994) and Morrison, Boroson & Harding (1994; hereafter MBH) announced discovery of a faint, luminous light distribution around NGC 5907, this galaxy was primarily known as a typical, edge-on Sc galaxy which happens to be near enough to us (V_{helio} = 667 km s^{-1} = 11 Mpc for H_0 = 65 km s^{-1} Mpc^{-1}) that we can study it in some detail. Previous observations by several groups (e.g. Sancisi 1976; van der Kruit & Searle 1981; Skurtskie et al. 1985; Sasaki 1987; Barnaby & Thronson 1992) had shown this galaxy to have both an HI and optical warp, but no obvious galaxy companions to produce this warp. As such, NGC 5907 became the prototype of the class of spiral galaxies having "non-interacting warps" (cf. Sancisi 1976).

The observations of Sackett et al. (1994) sparked new interest in this galaxy, in that they claimed to detect a significant halo around it. Two other groups then obtained deep surface photometry to try to study the halo in various passbands (Lequeux et al. 1996, 1998; Rudy et al. 1997). Our collaboration (the Beijing-Arizona-Taipei-Connecticut (BATC) Color Survey of the Sky (Fan et al. 1996) already had NGC 5907 as part of our galaxy calibration program. The BATC program uses the 0.6/0.9m Schmidt telescope at the Xinglong Station of Beijing Astronomical Observatory (the "BAO Schmidt"), with its focal plane equipped with a 2048 × 2048 Ford CCD. We have custom-designed a set of 15 intermediate-band filters to do spectrophotometry for pre-selected 1 deg^2 regions of the northern sky with this CCD system (cf. Fan et al. 1996).

Shang et al. (1998) summarize the main results of both our deep surface photometry and our Very Large Array[11] (VLA) 21 cm HI observations of NGC 5907: a) We detect a faint luminous ring around the galaxy, plausibly due to the recent tidal disruption of a nearby dwarf spheroidal galaxy. b) The HI map picked up a companion dwarf irregular galaxy, PGC 54419, on the side of one of the HI–warps and separated in radial velocity by only 45 km s^{-1} from NGC 5907. As such, we move NGC 5907 out of the category of "non-interacting" warped galaxies, but whether the observed interactions are sufficient to produce the observed warp is left for galaxy modelers to decide. c) Our HI observations suggest that the HI layer is higher near the center of the galaxy than at larger radii, suggesting this galaxy may also have a face-on warping of the disk.

[11]The Very Large Array of the National Radio Astronomy Observatory (NRAO) is operated by Associated Universities, Inc., under cooperative agreement with the National Science Foundation.

In this paper we present the details of our deep surface photometry of this galaxy, this time paying close attention to the issue of the faint luminosity distribution around this galaxy. Section 2 presents our observations, including details of the data reduction process, which are important for the reader to be able to critically assess the accuracy of our method. In Section 3 we study the faint luminosity distribution around NGC 5907 as it appears in our images, including how the ring, foreground stars, and a possible face-on warp can influence what we see. Our results are compared to those previously published in Section 4, in which we also reassess the likelihood of a halo existing around this galaxy. Section 5 summarizes the main results of this paper.

2. OBSERVATIONS AND DATA REDUCTION

The phases of data reduction that contribute to errors in the final image and over which we have some control are: bias subtraction, dark subtraction, flatfielding, sky background-fitting, star-masking, and photometric calibration. In this section we discuss these data reduction issues as they apply to the data we have obtained. When we compare our surface photometry to those of other observers (Section 4), we will find that, with few exceptions, our data are in very good agreement with published results.

2.1. Data Log and Preselection of Good Images

The observations of NGC5907 were obtained with the BAO 0.6/0.9m Schmidt telescope, using a thick Ford 2048×2048 CCD having 15μm pixels at the f/3 prime focus. The field of view of this CCD is $58' \times 58'$ and the scale is $1.71''$ per pixel. With this combination of telescope and CCD system, we can comfortably observe large extended objects and also get a sufficient amount of sky in a single frame. A large pixel size is better for finding low surface brightness features, as it minimizes the number of CCD pixels per surface area.

The images were taken with slight shifts between exposures ("dithered") so that cosmic rays and defects on CCD could be removed during the combining process. We employ the Lick Observatory data-taking system, which automatically subtracts the overscan of each image at readout time ("on–the–fly"), and records the overscan in the last column. We then process each program image through a series of software routines we term PIPELINE–I, which, among other operations, median-filters the original overscan and adds back to the image the difference between the original subtracted overscan and this filtered overscan.

In this way, the signal-to-noise (S/N) of the overscan is increased and any residual large-scale pattern produced in the image by imperfections in the overscan are removed.

Exposures of the field around NGC 5907 were made through two BATC filters: 6660Å (m_{6660}) and 8020Å (m_{8020}), whose band widths are 480Å and 260Å respectively (cf. Figure 1 in Fan et al. 1996). The BATC filters are designed to avoid contamination by the brightest and most variable night sky emission lines, producing a sky background of lower surface brightness obtainable under the same conditions in the broad band R and I filters. Use of intermediate bands also minimizes effective wavelength-related effects in the CCD sensitivity (Section 4.4).

137 frames of either 10m or 20m duration were obtained with the 6660Å filter on 23 nights from January 31, 1995 to June 27, 1995, all during moonless intervals at airmasses ≤ 1.5. The CCD was run with a gain of 4.1 e^-/ADU and a readout noise of 12 e^-. Similarly, 63 frames of 20m duration were obtained similarly with the 8020Å filter on 11 nights from May 26, 1995 to April 18, 1996, during which time the readout noise remained as before, but the gain varied somewhat. For the final combined 8020Å image the equivalent gain is 3.9 e^-/ADU. Of these 200 images, we selected the images for final reduction in the following manner (cf. Tables 1 and 2):

(1) Each individual frame was inspected visually to see if there are abnormal events that might affect photometry, e.g., traces of satellites crossing galaxy area, or visible problems with the bias overscan. If there was anything abnormal, the image was rejected.

(2) For each frame we measured the mean sky level, FWHM and flux for 20 isolated stars found in common on all frames. These values are shown in Figure 1 (and tabulated in Table 1) as a function of sequential image number for the 137 6660Å images, with flux and sky level normalized to an integration time of 20m. Those images having high stellar flux levels, low sky levels and reasonable seeing were selected for further study. A similar analysis was done for the 8020Å images (Table 2), with the net result that the final combined images are made of 84 6660Å frames taken on 15 nights and 50 8020Å frames taken on 8 nights. The total exposure time in the combined images is 26^h10^m (94200s) and 16^h40^m (60000s) respectively. The images which are used are listed in Tables 1 and 2 with their sky level counts, FWHM of stars and the mean counts (for 20m integration) measured for the 20 comparison stars.

2.2. Bias and Dark Subtraction

Biases measure the ADU level of zero second exposures and, as such are of low S/N individually. We took an average of 26 bias frames per night of observation using the IRAF task "imcombine", choosing the minmax algorithm in combination with the parameters "nlow" and "nhigh" set to 3 to reject bad points at $\geq 3\sigma$ level. As one test of CCD stability, we take 30 bias averages from a two month period during the observations and divide them into two sets of 15 bias averages each: BIAS1 from the first 15 bias averages; BIAS2 from the second 15. The difference, BIAS1–BIAS2 has a mean value of zero and no large-scale pattern exists, indicating good stability of our data-taking system. The average of BIAS1 and BIAS2, hereafter BIAS, is adopted as the final bias frame for correcting. It is equal to the average of 600 individual bias frames, has a mean value of about 1.2 ADU and a standard error of about 1 ADU/pixel (cf. Sec. 2.7).

Many dark frames must also be obtained throughout the observation sequence to reliably measure the dark current of the CCD. The dark count was obtained by obtaining forty, 20m dark frames over the same two month period. Subtracting BIAS from these frames yields a very small dark count of ~ 0.25 ADU/pixel/20m exposure. This summed dark count frame was then rescaled to the exposure time of, and subtracted from, each program image.

2.3. Large-scale Homogeneity of the Program Image

The first requirement in obtaining homogeneity over large-scales in a CCD image is to produce a very accurate flatfield map of the large-scale variations that exist in CCDs, and for those large-scale variations to be stable over periods of time long compared to the time over which the flatfield images and program images are obtained. This, in turn, requires controlling two factors: a) the DC stability of the CCD itself over the image area of interest; and b) the flatness of night sky and twilight, which, of course, are never really flat over $> 10'$ angles (see below).

A third factor affecting how well one can subtract the sky from the image of a galaxy is the fact that the quantum efficiency of a CCD pixel is a function of the effective wavelength of the radiation it detects. The one part of the data-taking process we *cannot* control is that the galaxies have different spectral energy distributions (SEDs) within the filters, and that these SEDs are different from that of the night sky.

While we cannot completely eliminate the systematic effects on the large scale homogeneity of any of these issues, we have taken steps to minimize their influence:

a. DC–stability: We can comfortably fit a galaxy as large as NGC 5907 ($14'$ in diameter) within the inner 25% of the CCD, which itself is in the inner 20% of the field of a Schmidt telescope. This eliminates issues pertaining to edge-effects in CCD flatfields and minimizes non-uniformity issues related to the optics of the telescope.

b. Flatness of the Flatfields: On a CCD chip covering essentially $1^\circ \times 1^\circ$ of the sky, neither the twilight nor the night sky will be flat over the whole chip (Wild 1997). This is obvious upon visual inspection of the twilight sky, when one takes into account that the field of view of our CCD is twice the size of the full Moon. It is also true on a cloudless, moonless night, as the airglow brightness correlates with air mass. Our eyes can easily detect gradients in twilight the size of the full Moon, and at a dark site, gradients in the sky over degree-sized scales. One might be able to devise a methodology of taking night sky flats at various airmasses and sky directions to minimize such gradients in the night sky, but such techniques are likely to be very time consuming, with no guarantee that sky gradients can be completely eliminated.

Rather, we take advantage of the special optical properties of a Schmidt telescope to construct a reliable flatfielding method that can employ a dome light. As detailed in Chen et al. (1999), we place a UV-transparent plastic diffuser over the correcting lens of the Schmidt. One dome light flatfield frame has more than 20000 ADU per pixel, corresponding to more than 84000 electrons (gain = 4.1). Twelve dome flats produce an overall flat field whose statistical pixel-to-pixel error is less than 0.1%. The diffuser ensures that the flux entering the Schmidt telescope is of a highly uniform nature. In the present paper, the proof of the accuracy of this flatfielding technique is demonstrated in two ways: by comparing noise in the division of average flatfields taken on successive nights to that expected from photon noise alone, and by the accuracy to which we can flatten the sky.

c. Color-related Effects: One of the factors leading us to decide to use intermediate-band filters for the BATC survey is the fact that SED-related quantum efficiency effects do exist in CCDs. Our own tests with stars (cf. Fan et al. 1996) show the measurements made in the two filters used here are insensitive to color changes in the program objects at the 1% level. Such is not necessarily the case for observations made with broad-band filters (Stetson 1990).

2.4. Rectification of the Summed Image

After the correction for the flatfield is applied, position offsets among the selected CCD frames were calculated with six plate coefficients and the position of the frame center, using the Guide Star Catalog of the Space Telescope Science Institute (Lasker et al. 1990). This process is done during the PIPELINE–I reduction process, and the derived plate coefficients are put into the FITS image header. After shifting all corrected images to a common center, bad pixels and cosmic-rays are rejected, and the cleaned images are combined to a single frame. We then redetermine the plate coefficients and plate center for the combined frames. The net images in the 6660Å and 8020Å filters contain 1928×1969 pixels and 1979×1979 pixels respectively. Figure 2a shows the combined image in the 6660Å filter, Figure 2b shows the combined image in the 8020Å filter.

2.5. Prediction of Background under the Galaxy and Ring

A reliable estimate of the surface brightness at faint levels near NGC 5907 requires us to be able to reliably determine the sky background under the regions of interest. These include not only the regions immediately adjacent to NGC 5907, but also for the ring which we found around it. This, in turn, means modeling the background formed not only by the night sky, but also by extraneous sources of light, including stars, other galaxies and, if present, Galactic "cirrus."

2.5.1. Star and Galaxy Masking

The stars and background galaxies to be subtracted on the combined image range from faint, near-point-sources of light to large regions contaminated by highly saturated stars. The traditional way to handle these sources of extra light is to mask them until their wings fall under a certain level, say, 10% of the variation in the sky. This is the procedure followed by MBH and Lequeux et al. (1996). We found that if we followed this procedure with our own combined images, we would be left with too few sky pixels from which to determine a reliable sky background. As a result, we proceed in a different, stepwise manner.

First, using DAOPHOT (Stetson 1987), we fit a point-spread-function (PSF) to each combined image. The fitted PSF is then subtracted from star images that are not saturated, following the prescription given in the 1987 Stetson paper and in the DAOPHOTII User's Manual. Saturated stars were not subtracted. Key to this process is as accurate a subtraction of the wings of the PSF as one can practically make.

The next step is to check the reliability of the PSF subtraction by plotting the residuals (obs−PSF model) versus distance from PSF center for each unsaturated star. The PSF–wings are subtracted cleanly for most stars and there is little remnant. However, the central areas of these subtracted stars show higher statistical fluctuations than the wings, owing to the higher original signal in the centers. While circular masks are placed over such cases, the size of the circles cover far less area than would have been the case if the whole PSF–wings of every star was masked.

The brightest, unsaturated stars are the exception to this second step, as the PSF-subtraction leaves a noticeable residual at faint light levels. Therefore, we treat both the brightest stars, saturated and unsaturated, the same, masking out the whole star to faint, but finite sky levels. In total, 117 bright stars in the 6660Å image were masked in this way.

Other galaxies that are resolved on our images are easily found via the DAOPHOT star-subtraction process, as the PSF-subtraction leaves a deficit of flux at the galaxy center surrounded by a bright halo. All background galaxies are masked entirely, but are generally so faint that these mask radii are small.

Figure 3 shows four results of the PSF-subtraction, including a saturated star, a bright unsaturated star fit by the PSF, a faint star fit by the PSF and for a faint galaxy fit by the PSF. The vertical lines indicate masking radii used. Our tests on all PSF-subtracted stars show that the residuals of the PSF-fits are less than 5 ADU on average, or approximately 5% of the statistical *noise* of the sky.

Treating saturated stars in these images is more problematic. The images of star which cannot be PSF-fitted due to saturation effects should, in principle, be wholly masked. Unfortunately, as stated earlier, if we tried to completely mask every bright star in our image, we would not be left with many pixels left in the image! As a result, we are forced to make two compromises in our star-masking procedure. First, we only mask each bright star to a surface brightness of 29th mag/arcsec^2. Second, owing to the optics of a Schmidt telescope, the PSF's of the stars are not symmetric anywhere in focal plane of our telescope. This is easily seen in Figures 2a and 2b of the present paper. However, the masks are, by necessity, symmetric. The net result is a slight mismatch of mask and PSF at very low light levels. As we will see, these compromises limit what we can do at faint light levels around NGC 5907.

In our 6660Å combined image, there are 7921 unsaturated objects detected among which are 1694 background galaxies in 1000×1000 pixel (1710″×1710″). We also note that, if one compares our 6660Å combined image with Figure 2 of MBH and Figure 1 of Sackett et al., it is clear that our observation is as deep, if not deeper, than theirs, detecting all of their stars, plus some fainter stars. Quantiatively, our

detection threshold is $3.5\sigma_{\rm sky}$, resulting in a limited magnitude of 23.3. This means that for $m_{6660} \leq 23.30$, $\log(N_{\rm star}) = 4.45$ deg^{-2} and $\log(N_{\rm galaxy}) = 3.88$ deg^{-2}. Star counts are overestimated, and galaxy counts are underestimated, as galaxies that are unresolved appear stellar, and galaxies with too low surface brightnesses are not found.

Separately, we mask out a circle of radius 250 pixels around the galaxy, as well as an area around the ring that is otherwise not excluded. This ensures that no galaxy-related or ring-related flux are included in the sky background determination, but it also means that the residual flux from bright stars masked in these regions is not modeled. The final masked 6660Å image is shown in Figure 4.

2.5.2. Sky Background Fitting

Once star-masking and galaxy-masking is complete, we can then attempt to model the sky background. Since it only makes sense to do this calculation near the galaxy and ring, we can safely limit ourselves to the inner 1000 × 1000 pixel areas ($28.5' \times 28.5'$) in each combined image, the region marked by the square in Figure 2a. This is also the region defined by our masking procedure (Figure 4).

First, we produced a smoothed version of each masked combined image by mode filtering each image with a box 10×10 pixels in size. To avoid contamination by masked pixels, only those pixels not in a masked area were used in calculating the mode in any box. This necessarily means that near each masked region, fewer pixels were used to generate the mode. After smoothing the mask regions whose radii are larger than box size are shortened and those whose radii are smaller than box size disappear. Once this smoothing operation is done, the original mask is reimposed on the image, thus eliminating the pixels which are in original masked areas. As a result of this process, edge effects from the masking procedure are removed.

We next experimented with the IRAF task imsurfit to perform fitting the sky background with various two-dimensional analytic functions. None of these models was found to be wholly satisfactory, owing to the fact that we have to restrict the fits to low order polynomials to avoid introducing spurious interpolations in the masked regions. In every case, we could see large areas of the image that were systematically underfit or overfit. Low order spline fits similarly suffer. At the end, we settled on a stepwise method that works reasonably well when faced with a large part of the image masked-out.

We fit each row of the smoothed-and-masked image with a one-dimensional Legendre polynomial of low order. In doing this fit, we reject points above 2σ on the high side and 3σ on the low side, as well as

all pixels inside the mask. The reason for the asymmetric rejection of points is that the main sources of scatter on the high side are faint, undetected sources and unfitted faint wings of stars, while the low side values result from statistical fluctuations. This is clearly seen when you make histograms of the pixel values in the masked images; the histograms are skewed towards positive values. Necessarily, this process requires interpolating each line under the galaxy/ring mask, keeping the order of the Legendre polynomial to be 3 or less.

The row-fit to the smoothed 6660Å image is shown in Figure 5a. Next, we repeat this process in the column direction (Figure 5b). This ensures we are predicting the sky underneath the galaxy in a mutually orthogonal manner. The row and column fits are then averaged (Figure 5c), and this average image is smoothed with a circular Gaussian of $\sigma = 30$ pixels, truncated at $\pm 4\sigma$. The final smoothed image was adopted as the sky background (Figure 5d).

The 6660Å image with its fitted background subtracted is shown in Figure 6a and the 8020Å image is shown in Figure 6b. As is evident, even with our best attempt at star-subtraction and masking, one can still see faint, partial rings near many of the brighter stars. These rings are at surface brightnesses 29th mag arcsec^{-2} and fainter in the 6660Å image. As stated earlier, this end result is a compromise, for if we were to truly exclude all starlight from this image, very little would be left of the image from which to determine sky, and in many of the MBH cuts, leaving little or net flux to examine. As is plain, NGC 5907 is at a Galactic latitude (51°) where stellar crowding starts to seriously affect what one can quantitatively do at low surface brightnesses. As a check of the accuracy of our background fitting and masking procedures, we have taken four averages of 30 rows ("slices") each through the background-subtracted 6660Å image (Figure 7) and similarly-processed 8020Å image (Figure 8) that span the region of interest around NGC 5907.

At the tops of each panel of Figures 7 and 8 are given these sky-subtracted slices through the galaxy. At the bottom of each panel are given the residuals of the subtracted sky background for each slice. The upper line is the residual of our sky fitting and subtracting procedure, while the lower line is the residual of normal two-dimensional function fitting. They are shifted down by 110 ADU and 150 ADU seperately for display purposes. It is obvious that our procedure produces smaller residuals than two-dimensional function fitting. From Figures 7 and 8 a reader of this paper can check as to whether our sky subtraction procedure introduces any spurious features into the sky-subtracted image. The lower parts of these panels also demonstrate that our sky-subtraction procedure conservatively fits an effective two-dimensional plane under the masked region around the galaxy.

Of course, no sky background fit is perfect, and it is these imperfections that contribute to the limit to which one can do accurate faint surface photometry. To estimate the systematic error from this source, we sample 381 areas of 50×50 pixels of the background-subtracted 6660Å image and calculate the mode value of each area. After excluding areas in the region severely affected by masking, the standard error of these mode values is 18 ADU. We take this as our best estimate of the irreducible 1σ accuracy of our sky background fit. In a similar manner we determined the accuracy of the sky background fit to be 17 ADU for the 8020Å image.

In contrast, if we had limited our sky background fits to only those obtained by analytical 2-dimensional functions, the row slices showed many more systematic variations and the 1σ systematic error was typically 30 ADU. We believe our method of sky background fitting produces a reliable match to what is, inherently, a very lumpy sky at very low light levels.

2.6. Zero Point Calibration

It is standard practice for BATC observations to use Oke–Gunn (1983) standard stars as our calibration stars when the night is photometric. The nights of 06March95 and 01April96 in the series taken for NGC 5907 were photometric. The magnitude zero point for each combined image corresponds to a flux of 1 ADU/second is: 19.08 ± 0.01 mag for the 6660Å image; 17.79 ± 0.01 mag for the 8020Å image. The sky brightness values are 21.26 mag arcsec^{-2} and 19.91 mag arcsec^{-2}, respectively. The parameters we derive for these two combined images are given in Table 3. Note that the FWHM of the PSF of the combined images (2.3 and 2.5 pixels, or $2''$ in radius), is worse than typical seeing of $2''$ at the Xinglong Observation Station of the Beijing Astronomical Observatory, using the Schmidt telescope (cf. Figure 1).

2.7. The Estimated Errors we Can Control

The random error per pixel is given by the random error in photoelectrons, not in ADU. In the case of the 6660Å image, there are 4.1e$^-$/ADU, and 3.9e$^-$/ADU for the 8020Å image. Hence, if a pixel has n ADU, this corresponds to $4.1n$ e$^-$ for the 6660Å image, and the error is $\sqrt{4.1n}$ in e$^-$, equivalent to an error of $\sqrt{n/4.1}$ in ADU. In the case of the 8020Å image, the error would be $\sqrt{n/3.9}$. The sources of error in our images we can estimate are: readout noise; photon noise per pixel; noise in average bias; noise in average dark; noise in flatfielding; systematic errors in the sky background mapping. Note that all of these

noise levels save two (systematic flatfielding errors and systematic sky background errors) can be reduced by increasing the number of pixels sampled.

Readout noise: Random noise from readout comes from a readout noise (in terms of error of the mean) of 12 e^-/pixel per image. In the case of the 6660Å combined image (84 input images) this is $12\times\sqrt{84}$ ≈110 e^-/pixel; $12\times\sqrt{50}$ ≈85 e^-/pixel for the 8020Å image (50 input images). From above, the noise in the readout is 26.8 ADU/pixel for the 6660Å image and 21.8 ADU/pixel for the 8020Å image.

Photon noise per pixel is given simply as $\sqrt{n/4.1}$ ADU for the 6660Å image and $\sqrt{n/3.9}$ for the 8020Å image.

Bias and Dark: Because the ADU/pixel counts of the average bias and dark are very small, the main error comes from the readout noise, and is 3 ADU/pixel. The final bias image used for bias subtraction was an average of 600 single bias frames, resulting in a noise of 0.12 ADU/pixel. The error transmitted into the combined image in 6660A is $0.12\times\sqrt{84}$ ∼1 ADU/pixel. The error introduced by dark-subtraction is also about 1 ADU/pixel for both passbands. Compared to the photon noise of night sky and readout noise of the program images, the errors introduced by biases and darks are thus negligible.

Flatfielding As is evident from Figures 7 and 8, our flatfielding procedure produces a flat enough image that the structure in the background is dominated by the intrinsic lumpiness of the faint night sky. This is consistent with the tests we have done to confirm the validity of our flatfielding procedure (Chen et al. 1999). However, from the flatfield we do have some pixel-to-pixel noise due to photon statistics. For each filter, 12 frames of dome flatfields, each with more than 20000 ADU, are combined together to make the final flatfield image. Thus, the photon noise in the flatfield is $\sqrt{20000/4.1}/\sqrt{12} \sim 20$ ADU or 0.1%. Since the final galaxy image was combined from 84 dithered frames, the error was reduced by $1/\sqrt{84}$ to 0.01%, approximately. For the 8020Å image, it is about 0.015%.

Given the changes in flatfield pattern night-to-night, run-to-run in a typical CCD system, we separately check the large-scale uniformities of our flatfields by dividing the combined flat-fielding frame of one night by that of the adjacent night. 9 divisions of flatfields taken in the 6660Å band have an average pixel-to-pixel variation of 0.16%, indicating that the noise of the combined flat-fielding frame of one night is about 0.11%. This value is consistent with 0.1% predicted by calculating photon noise, showing our flatfields are very stable from night-to-night. As such divisions also included any large-scale pattern changes in the flatfield, this test also shows that the large-scale pattern is reproduced very accurately with the dome/diffuser technique for a Schmidt telescope. When we then smooth the flatfield ratios by binning up pixels, we find

that the large-scale variation is about 0.026%. Therefore, the large-scale error of the combined flat-fielding frame of one night is slightly smaller than 0.02%.

Intrinsic variation in galaxy brightness: MBH point out that the intrinsic variation could be expressed by the formula given by Tonry & Schneider (1988), assuming $\overline{\mathrm{M}}_R = 0$ (Tonry et al. 1990). In our case, $\mathrm{m}_1 = 19.08$ mag, an exposure time of 94200s, a distance of 11 Mpc (assuming H_0=75). Since the central wavelength of our 6660Å band is similar to R band and the difference between our 6660Å band and R band is small (Sec 4.1), a value of $\overline{\mathrm{M}}_{6660} = 0$ should be a reasonable assumption. This gives an estimated variance of 3.3g, where g is the mean number of counts due to the galaxy only. So 45 ADU/pixel (equal to 28.5 mag/arcsec^2) will give an error of 12 ADU/pixel, far less than the photon noise of night sky of 95.1 ADU/pixel. The estimated variance of that in 8020Å image is 1.6g (assuming $\overline{\mathrm{M}}_{8020} \sim -1$, when $\overline{\mathrm{M}}_R \sim 0$ and $\overline{\mathrm{M}}_I \sim -2$ (Tonry et al. 1990)). For 22 ADU/pixel (equal to 27.5 mag/arcsec^2) we get an error of 6 ADU/pixel, small compared to our other sources of random error.

2.8. The Total Error Budget

Random Noise: Of the photon noise of night sky, readout noise, bias/dark count errors and flatfielding random errors, the reducible random errors in a blank sky area are dominated by the first, and are estimated to be close to 100 ADU/pixel for the 6660Å image and 83 ADU/pixel for the 8020Å image, which are roughly consistent with the σ measured directly from the combined images (cf. Table 3). These noises and intrinsic variation of the galaxy can be reduced by binning adjacent pixels. As the distance from the galaxy plane increases, the bin size increases exponentially to keep similar S/N ratio. As an example, the bin size is 45×59 pixels at the farthest distance, and the random noise is reduced to only 2 ADU.

Large-scale Error of Flatfielding: Both from the tests we made above, and those made by Chen et al. (1999), the large-scale error of BATC flatfielding is less than 0.1% (Chen et al. 1999). Since we combined 84 frames for 6660Å band and 50 frames for 8020Å band, the error introduced by this source is reduced to about 0.01%.

Systematic Error of Background Subtraction: In the previous section we found that the irreducible scatter in the images is 18 ADU for the combined 6660Å image and 17 ADU in the combined 8020Å image. Taken together with the sources of random errors, this places an intrinsic accuracy of 20 ADU/pixel for faintest signal in the 6660Å image and 19 ADU/pixel in the 8020Å image *where we can*

explicitly fit the sky. Expressed in terms of surface brightness units, these errors correspond to a surface brightness of 29.4 mag arcsec^{-2} in the 6660Å image, and 27.7 mag arcsec^{-2} in the 8020Å image. In masked regions, this intrinsic error will be larger and more systematic, owing to residual surface brightness around the masks of bright stars.

Residual Foreground Star Subtraction: The slight imperfections of the star masking process can be estimated from the slices in Figures 7 and 8. By examination of the regions around the brighter subtracted stars, it is apparent that residual star light affects our image at the level of 20–50 ADU/pixel in specific places around most of the brighter stars. From above, this is at surface brightnesses around the 29th mag arcsec^{-2} level in the 6660Å combined image. It is also evident from Figures 7 and 8 that if we tried to mask the stars to fainter light levels we would, indeed, be left with very few remaining pixels in these cuts. The complications in our analysis of these data that this compromise brings are discussed below.

The sources of variation in our surface photometry in 6660Å that are generally present in our 6660Å combined image are summarized in Table 4. This example assumes we are observing a surface brightness that gives us 50 ADU counts from the galaxy, 37066 from the sky and bin size of 45×45 pixels. We choose this bin because it lies at the envelope of the galaxy halo. It can be found that a combination of irreducible systematic error of determining sky background, plus unavoidable imperfect star–masking, determine the ultimate limit of the accuracy that can be achieved.

In reality, to this value (24 ADU) we must add the more problematic residuals that we see around bright stars within the masked-out region around the galaxy and ring. At its lowest level ($\sim$ 20 ADU), the error is comparable to our minimum error; at its highest ($\sim$ 50 ADU), it dominates the minimum error. As we will see, residual surface brightness from bright stars likely poses the ultimate limit to which we can investigate the halo of NGC 5907.

3. SURFACE BRIGHTNESS DISTRIBUTION OF, AND NEAR, NGC 5907

3.1. Color and Magnitude of NGC 5907

We measure the total magnitude of NGC 5907 to a surface brightness of 27 mag arcsec^{-2} of $m_{6660} = 9.9 \pm 0.02$ and $m_{8020} = 9.5 \pm 0.02$. To obtain these values we replaced the areas excluded due to foreground stars with the mean value of the surrounding background. To put this into more standard terms, we use the fact that we find an average transformation of $R - I = m_{6660} - m_{8020} - 0.2$ mag, based

on comparison with existing surface photometry of NGC 5907 (Sec. 4.2). Thus, our observations indicate NGC 5907 itself to have $R - I = 0.2 \pm 0.04$. If we exclude a rectangle around the obvious dust lane in this galaxy, we find the average R–I color to be -0.1 ± 0.1. This bluer color refers to the average value for stars less-affected by dust in the disk, and is typical of a stellar population dominated by younger stars.

3.2. The Edge-on Stellar Warp

The HI warp of NGC5907 first found by Sancisi (1976) is strongly confirmed by our own VLA 21 cm HI observations (Shang et al. 1998). Given the warp in the HI gas, it is logical to search for an analogous warp in the stars. While van der Kruit (1979) only had marginal evidence for such a stellar warp, Sasaki (1987) claimed to detect an optical warp at a projected radial distance along the major axis from 13.3 kpc to 24.0 kpc from the center of the NGC 5907. Sancisi (1993) showed that there are similarities between the optical warp of Sasaki and the HI warp. In Figure 7 of MBH, there is evidence for the start of a stellar warp at 4.1 kpc from the center of the galaxy.

The warp in each of our combined images is determined by measuring the horizontal distances between the surface brightness profiles of two sides of the galaxy around a fiducial position angle, and measuring their mean offset as a function of distance along the galaxy major axis. Figure 9 shows the optical stellar warps calculated from our brightness profiles parallel to the minor axis. We find a warp in the galaxy that begins near the center of the galaxy (at 4.1 kpc, in agreement with what MBH found) and changes continuously outward to at least 16 kpc from the center, such that at a radius of 16 kpc, the warp deviates about 0.4 kpc ($\sim$ 4 pixels) above the average galaxy plane. We see the same warp in both our 6660Å image and in our 8020Å image.

In regards to investigations at high latitudes for faint surface brightness in an edge-on galaxy, warps are likely to occur with greater frequency along the line-of-sight to the disk than at the disk edges, given relative angular coverage. Given that a galaxy disk is seen to have a warp at its edges, it increases the possibility that the galaxy is also warped along the line-of-sight. This face-on warp may distort galaxy surface brightnesses at large z-distances from the galaxy plane in a non-axisymmetric way, as opposed to the expected symmetry from a halo. As such, separating the two kinds of possible sources of high-z surface brightness is, in principle, possible. Relevant to this issue in the case of NGC 5907, we note that there is some indication in our current VLA observations, that the HI layer is higher near the center of the galaxy than outside the center (Shang et al. 1998). We explore the consequences of this hypothesis below.

3.3. The Stellar Ring

As shown in Shang et al. (1998) and has been evident in the deep images we present here (Figure 6a,b), NGC 5907 has a faint, luminous ring around it. Our schematic for this ring is shown in the inset in Figure 6a. As discussed in Shang et al. (1998), the ring is reasonably elliptical in shape, of similar angular size as NGC 5907, and the center of NGC 5907 is near one focus of the ellipse. The reality of this ring has been confirmed on other CCD images (cf. Shang et al. 1998), and part of the ring can be faintly seen in Figure 3 of MBH (although they do not recognize it as part of a ring). The various arguments for the origin of this ring are made in Shang et al. (1998), from which we conclude that by far the most likely interpretation is that of a dwarf spheroidal galaxy in the process of being torn apart by a strong tidal encounter with NGC 5907.

The physical particulars of the ring indicate that the luminosity distribution within it is irregular both in surface brightness and in apparent thickness. The maximum width of the ring is found at the NE end of its major axis (40 pixels = $68.4''$ = 3.6 kpc at the distance of NGC 5907), while its smallest width is found near the region where the ring overlaps NGC 5907 (20 pixels = $34.2''$ = 1.8 kpc). In our estimate of the total brightness of the ring, we are limited by masked areas within NGC 5907 itself obscuring that part of the ring nearest the galaxy. As such, we can only unambiguously measure unmasked pixels of the ring only in its clearer NE half. We find the average surface brightness in the NE half of the ring to be 28.0 ± 0.3 mag arcsec^{-2} in the 6660Å image and 28.3 ± 1.8 mag arcsec^{-2} in the 8020Å image. The much larger error for the ring surface brightness at 8020Å is expected, given our error budget estimate (Sec. 2.8). If we assume that the whole ring has this average surface brightness, we obtain total magnitudes of $m_{6660} = 14.7 \pm 0.3$ mag and $m_{8020} = 15.0 \pm 1.8$ for the ring. However, these estimates may be brighter/fainter limits to the brightness of the ring, as it is not obvious how irregular is the light distribution in the regions we cannot investigate due to overlap with the galaxy and with foreground stars.

The larger error on m_{8020} precludes quoting a reasonable color for the ring as a whole. If we measure just the highest surface brightness features in the ring (denoted by arrows in Figures 8 and 9), we find 26.8±0.1 mag arcsec^{-2} in 6660Å and 26.1±0.2 mag arcsec^{-2} in 8020Å, yielding a color index $m_{6660} - m_{8020} = 0.7 \pm 0.3$ (or $R - I = 0.5 \pm 0.3$). In order to confirm this result, we also measure the total flux within the brightest area of the ring by (indicated by the parallelogram in Figure 6a) to give an average surface brightness of 27.0±0.1 mag arcsec^{-2} in 6660Å and 26.4±0.3 mag arcsec^{-2} in 8020Å, implying an R–I color of 0.4±0.4. Measurement of the second brightest area of the ring also gives a similar result. On

average, we measure the ring to have an R–I color of 0.5±0.3, consistent with the R–I colors for Galactic globular clusters of metallicities [Fe/H] ~ -1.0 (cf. Peterson et al. 1993).

3.4. Cuts Perpendicular to the Disk

In Figure 6a we show how the perpendicular cuts used by MBH are related to our combined 6660Å image. (Rather than term these as cuts "along the minor axis," we prefer to designate these as cuts "perpendicular to the major axis.") As did MBH, we designate each cut by a letter and number, with A being the central cut, B1 and B2 being the cuts nearest the center (1 to the northeast, 2 to the southwest), and D1 and D2 being the cuts in the outer parts of the galaxy.

To increase S/N along these cuts we bin 45 pixels in width and, to keep this S/N approximately constant, we increase the heights of the bins exponentially with z distance from the galaxy plane, with 1 pixel being the smallest height, and 59 pixels being the largest. This procedure is directly analogous to that employed by MBH. For our estimate of galaxy surface brightness, we take the mode of each bin sampled. The reason for this is that undetected background sources, plus residuals from the star masking procedure, will tend to upward bias the mean and median ADU counts tabulated in each bin. We experimented with alternate definitions of the flux in a bin and found that, while σ clipping algorithms can partly resolve this problem, the best way is to use mode value instead of mean or median. A σ clipping algorithm is used to eliminate bad pixel values (of which a few still remain in the combined image) from the histograms.

The perpendicular profiles we derive from the 6660Å image are given in Figure 10 and in Figure 11 from the 8020Å image, and are tabulated in Table 5 for completeness and to aid in future studies of this galaxy by others. The profiles of the two sides (NE and SW) about the galaxy plane are folded around the curved warpline to remove the effect of the edge-on warp. Those parts of the profiles fainter than $m_{6660} = 29$ and $m_{8020} = 28$ (about 0.1% of sky) are not presented since their values are uncertain by over 1 mag owing to the finite size of our limiting systematic errors. The coding of the symbols used to plot these perpendicular profiles is such that solid symbols represent parts of the profile *not* influenced by the surface brightness distribution in the ring (Shang et al. 1998), while open symbols are those part of profiles in which the ring light, and a possible warp in front of the galaxy, influences what we see.

It is obvious that at large z-distances from the plane of the galaxy, the faint surface brightness distribution in the 6660Å image around NGC 5907 *is not symmetric about the midplane of the galaxy.* Only

in the case of the A and C2 cuts are the profiles on the NE and SW sides of the galaxy consistent within the errors at faint surface brightnesses. The NE sides of the profiles in cuts C1, D1 and D2 are systematically brighter than the SW sides in these cuts. In the case of cuts B1 and B2, one side is brighter than the other, but the sense of asymmetry changes from B1 to B2. The B1 profile (to the NW of the galaxy center) has its NE side significantly brighter than the SW side, while the B2 profile (to the SW of the galaxy center) has its SW side equally brighter than the NE side as for the B1 profile. Larger errors at faint levels in our 8020Å image preclude any such conclusions being separately made for the cuts in this image.

Thus, on the basis of what we see in our 6660Å image, we find that the faint surface brightness distribution around NGC 5907 is asymmetric. With these data, we can confidently rule out the presence of a halo in this galaxy beyond a distance of 5 kpc.

3.5. Ring, Foreground Stars and Possible Warp influences on the Asymmetry of the Perpendicular Profiles

As can be seen by comparing the perpendicular profiles in Figures 10 and 11 to the positions of the cuts relative to the ring in Figure 6a, cuts C1, D1 and D2 all intersect the ring on the NE side of the galaxy. What confusion with the ring can do to the perpendicular profile is also seen in Panel 1 of Figure 7. The apparently smooth gradient in the outer profile of the galaxy (from pixel numbers 600 to 750) is due almost entirely to the presence of the ring in this region (cf. Figure 6a).

If we conservatively take the average surface brightness of the ring (28th mag/arcsec^{-2}; in the 6660Å image; see Sec. 3.3) as our estimate for the ring surface brightness near the galaxy, then most of the faint extensions seen in cuts C1, D1 and D2 on the NE side of the galaxy can be attributed to ring light. Separately, as we can make a prima facie case that the ring is elliptical in shape and has the center of NGC 5907 at one of its foci (cf. Shang et al. 1998), it is difficult to disentangle true galaxy light from possible ring light in the A cut on the SW side of the galaxy at surface brightnesses fainter than 28th mag/arcsec^{-2} in the 6660Å image.

Of the remaining 3 of the six non-centered (B,C,D) cuts made, C2 has the least foreground star contamination, but still has some star contamination on its SW side. In contrast, both B1 and B2 include large sections of the masks around bright stars: B2 on its SW side, B1 on its NE side. Similarly C1 on its NE side, D1 on its NE side, and D2 on its SW side. Interestingly, in every case, the side of the galaxy

that is brighter is more foreground star-contaminated than its partner. This would strongly suggest that residual star light at low light levels (surface brightnesses of 29th 6660Å mag arcsec^{-2} and fainter) is are contributing to the differential effect in these cuts seen at surface brightnesses of 28th 6660Å mag arcsec^{-2} and fainter.

On the other hand, *if* this galaxy has a face-on warp, one might expect that the warp would give an asymmetrical distribution perpendicular to the center of the disk near the galaxy center, i.e., in cut B1 versus cut B2. While such an effect is certainly seen, the apparently irreducible effects of foreground star contamination make it highly unlikely that we will be able to unambiguously detect a face-on warp in this galaxy, even if it exists. NGC 5907 simply has too many foreground stars around it to be a good edge-on galaxy candidate in which to find a face-on warp.

4. Comparison with Previous Results

4.1. Comparison to the Results of MBH.

In order to do a close one–to–one comparison to the published results of MBH, Dr. H. Morrison kindly sent us the surface brightness data they used to make their perpendicular cut diagrams in the MBH paper (data which were not published in their paper). We list these data in Table 6 in the same manner as we did for our own data. If we compare the broad-band R surface brightness profiles from MBH given in Table 6 to our own 6660Å surface brightness profiles given in Table 5, it is apparent that, for similar errors, our data go ~ 1.5 mag fainter than those of MBH. The main reason for this is that the sky is much fainter in our intermediate band filter (which avoids the brightest night sky lines) than in the broad-band R filter used by MBH: 0.6 e$^-$ s^{-1} arcsec^{-2} in our combined 6660Å image to 7.4 e$^-$ s^{-1} arcsec^{-2} quoted by MBH for their R-band data.

As is evident from the graph presented in their paper, Sackett et al. combined NE and SW sides of each cut to form one combined perpendicular profile per cut. With our higher accuracy at fainter light levels, we can see the asymmetry in the faint light distribution perpendicular to the disk that MBH and Sackett et al. could not.

We compare the perpendicular profiles of MBH to our 6660Å image profiles in Figure 12. A zero point of 0.3 is added to the R band data of MBH to bring the two filter systems onto the same photometric system at bright levels of the galaxy. While we note that MBH cite results only for R band surface brightnesses

brighter than 27th mag arcsec^{-2}, the actual data given to us by Dr. Morrison go fainter than this. As neither MBH or Sackett et al. give actual surface brightness profile information, we choose to use the data sent to us by Dr. Morrison as the basis for our comparison.

We find generally good agreement with MBH data, even at low light levels, in most cases. Good agreement is found between our data and those of MBH, both in form and zero point, for distances less than 5 kpc from the galaxy midplane in all cuts. This gives strong support to accuracy of the zero points obtained by both us and MBH, and to the fact that our perpendicular profiles are similar, typically at surface brightnesses brighter than 27th mag arcsec^{-2}.

Above a distance of 5 kpc from the galaxy midplane, the comparison must take into account the asymmetry of the faint light distribution seen. Namely, for the cuts B1, B2, C1, D1 and D2, the two faintest measurements of MBH are likely measuring only the brighter flux from one side of the galaxy (else, we should see the MBH data to be 0.75 mag fainter than ours owing to this asymmetry). This is consistent with what we see in Figure 12, in which the faintest MBH measurements are in accord with our brighter surface brightnesses measured on one side of the galaxy or the other. The two exceptions to this agreement at low light levels are the A and C2 cuts, where the surface brightness difference systematically occurs at levels 27.5 mag arcsec^{-2} and fainter in these two cuts.

This comparison would strongly suggest that as well as in our data, the surface brightness profiles determined by MBH are affected by residual foreground star subtraction at very low light levels. Inspection of Figure 3 of MBH, and the higher resolution modeled figure in Sackett et al., show this to be the case. One can see extra flux around the brighter masked stars in a similar kind of asymmetric pattern as we see in our own masked 6660Å image (Figure 6a). In addition, the two bright stars that are at the lower left from the galaxy in their image show CCD bleeding along the columns that is not completely taken out by their masking procedure.

Thus, we conclude that our data, both in zero point and in form, are in good agreement with the data of MBH at low light levels. Differences that are seen are as likely to be attributable to issues pertaining to foreground star subtraction as to any other kind of systematic error. From this we conclude that the data used by MBH and Sackett et al. for their investigations into the possible thick disk and halo of NGC 5907 were as contaminated as ours by ring light and residual light from masked foreground stars.

4.2. Comparison to the Results of Lequeux et al. and Rudy et al.

The J, K, V and I surface brightness gradients in NGC 5907 are given in Rudy et al. (1997) for both their observations (J and K) and those of Lequeux et al. (1996) (V and I). The additional B observations of 1998 do not have published numbers. In comparing these data to our own, we first need to determine if the surface photometry was deep enough to detect the ring around NGC 5907. In the case of MBH, the answer is yes (Sec. 4.1).

Of the observations of Rudy et al. (1997) and Lequeux et al. (1996), the evidence as to whether the Rudy et al. (1997) data did go faint enough to detect the ring in the near IR is inconclusive. Rudy et al. do remark that their surface brightness profiles show an asymmetry, with the NE side of the galaxy having more light at low levels than the SW side. However, neither we nor MBH see this bump in our data. In the case of Lequeux et al. (1996), it is apparent both from the image and the surface brightness profiles they give that their observations did not go faint enough to detect the ring.

We compare the perpendicular profiles along the minor axis of NGC 5907 in the 8020Å image to that given by Lequeux et al. (1996). for the I band, and by Rudy et al. (1997) for the J and K band, in Figure 13, and tabulate these data in Table 7. The zero point shift in the I band is 0.1, implying a zero point shift between $m_{6660} - m_{8020}$ and $R - I$ of about 0.2.

There is generally good agreement among the J, K and 8020Å perpendicular profiles within the quoted errors. The one exception is the presence of the above–mentioned "bump" on the NE side of the Rudy et al. J and K data that is not present in either our data, those of MBH (cf. Figure 12, A cut) or those of Lequeux et al. This indicates little detectable color gradients in colors can be formed from these three passbands, although the mutual errors are large enough to hide a significant color gradient, if it does exist here. The absence of quoted errors for the Lequeux et al. I band data preclude an accurate assessment of agreement/disagreement. Even so, within the cited errors of the other data sets, one finds differences between the Lequeux et al. I band perpendicular profile and those of the other data sets only in the inner NE 3 measured points. In contrast, the J, K and 8020Å data for these three measured points are in very good agreement. Once again, exactly how each group has handled the foreground star contamination problem likely leads to the differences seen in the inner part of the profile shown in Figure 13.

4.3. Colors of NGC 5907 Perpendicular to its Disk

As is evident from the above comparison with other data, it is very difficult to obtain reliable colors of galaxies at faint surface brightnesses. The errors of both passbands involved in forming the color quadratically combine, and the resulting color differences are often small relative to this error. Such is clearly the case for the color gradients we can form perpendicular to the disk of NGC 5907 in the $m_{6660} - m_{8020}$ color we can form from our data, as shown in Figure 14. The error bars are formal 1-σ errors per measurement. Since in these data 2-σ to 3-σ errors are likely present as well, it is apparent that the color gradients 4 kpc and greater from the disk of NGC 5907 are completely dominated by observational error.

Interestingly enough, within 4 kpc of the galaxy plane, we find that in many of the cuts the color gradients become bluer in $m_{6660} - m_{8020}$ with increasing radius, with cut D2 being the notable exception. In D2 alone, the color gradient, on both sides of the galaxy, seems to get *redder* with distance from the midplane.

As can be seen also in Figure 13, colors formed outside the 4-kpc midplane region from any of the published passbands show little difference within the mutual errors of observations (save for the questionable NE bump in J and K in the Rudy et al. data).

4.4. The Limiting Factors in Faint Galaxy Surface Photometry

We have already detailed the three sources of systematic error in faint galaxy surface photometry — systematic errors in determining the flatfield, systematic errors in determining the sky background, residual surface brightness from bright stars that one cannot easily mask. Most observers try to take these factors into account (although not all explain that they do in their papers; cf. Lequeux et al. 1996; 1998). However, there are two other sources of zero point errors in sky level determination that are not discussed in the previous papers. We include these now to complete our discussion of the data.

First is the fact discussed above that CCDs have wavelength-dependent quantum efficiencies and this dependence is slightly different from pixel to pixel. Galaxies and sky background can have very different colors, depending on which part of the spectrum is observed, how bright the night sky lines are, how bright the sky continuum is, etc. If the difference in color is sufficient to change the effective wavelength of a filter enough to change its quantum efficiency in a detectable manner, the sky level estimated will be affected in

direct proportion to the percent change in QE. Take the R band observation as an example, since the galaxy effective wavelength could be off by 50–100Å from the sky effective wavelength in the broad-band R, it is entirely possible that the QE of the CCD could differ by 1 part in 1000 from galaxy effective wavelength to sky effective wavelength. The zero point of the B, V and I observations are similarly affected.

The issue for J and K observations are somewhat different, as there the sky level is so bright that it is a triumph of instrumentation that one can get a good estimate of sky down to less than 0.01% accuracy. Again, however, if the IR Array QE is a function of effective wavelength, accuracy in estimate of sky background in the broad band J and K filters will be limited by the difference in QE between galaxy color and sky color.

We chose intermediate-band filters for the BATC survey for several reasons, but one of the chief ones was to limit the bandpass sufficiently that differences in color of the objects observed would not produce significant differences in the effective wavelength of the filters. In the case of the 6660Å and 8020Å filters, we designed them to avoid the brightest (and most variable) night sky lines. As such, we believe the change in QE between galaxy and sky in our filters is much less than in the broad-band filters. A separate advantage, of course, is in a concomitantly much lower sky background (12 times lower in the 6660Å filter than MBH obtained at KPNO in the broad-band R).

The second source of non-modeled zero point error is the photometricity of the telescope field of view and the inherent non-flatness of the night sky. All telescopes suffer from optical imperfections, most of which affect the transmission of light from the sky as a function of distance from the center of the field. It is primarily for this reason that the flatness of the night sky has become the final arbiter of how well the CCD image has been calibrated. Yet, the night sky itself is not flat, which is pointed out by Wild (1997). In our degree-sized BATC CCD fields we clearly see the gradient of the night sky getting brighter towards lower altitudes. With CCD arrays getting to be degree-sized and greater, this problem is only enhanced. While one takes many separate sky images at different times of night — so the altitudinal gradients go in different directions on the CCD — in the end the cancellation of the gradients cannot be perfect. Any residual gradient in the sky will then be mistaken as a gradient in the sensitivity of the CCD itself, and mistakenly divided out. It should be subtracted out of the image, as we have attempted to do in the present paper.

One advantage of using a Schmidt telescope for the BATC survey is that we position the CCD in the center 1° of a focal plane that has been specifically optimized to give as flat a field of view as possible in the center of a 6° radius circle. Such is true for any Schmidt telescope, which is one reason they are noted

for giving the most reliable sky background estimates of any type of telescope.

The bottom line is that all sources of error conspire such that it is extremely difficult to obtain sky background estimates and large-scale uniformities to accuracies better than 0.1% of the sky level. In defense of our results, we can point to much lower sky level and narrower passbands.

4.5. Does NGC 5907 Have a Halo?

Two facts are clear from the above analysis: 1) Our data substantially agree with the data in the literature for the surface brightness distribution seen perpendicular to the disk of NGC 5907. 2) We find the light distribution perpendicular to the disk of NGC 5907 to be highly *asymmetric* about the galaxy midplane, with one side enhanced relative to the other in each MBH B, C and D cut.

The difference between the present data set from those previously published is a combination of the advantage of using the center field of a Schmidt telescope as well as intermediate-band filters. The use of the intermediate band filters resulted in a much fainter sky; the large field of view of the Schmidt permitted features such as the ring to be easily identified. The large angular pixel size of our CCD (1.71″/pixel) is an advantage when searching for faint surface brightness, as we minimize the number of pixels per large surface area.

Since we measure the ring around NGC 5907 to have an average surface brightness of 28th 6660Å mag arcsec^{-2}, one can see from the images themselves, Figures 2a and 6a, that NGC 5907 does not have a halo at these faint surface brightnesses. This fact is more clearly evident on the SW side of the galaxy, the side away from the bulk of the ring.

We are forced to the conclusion that asymmetries in foreground star PSFs lead to extra light around star masks, which combine with ring surface brightness to produce what faint extensions of surface brightness we see in the MBH cuts. This is due to the fact that the asymmetries in the surface brightnesses derived from our images in the MBH cuts correlate with the degree of foreground star contamination in four of the six non-centered cuts. Overlap with the ring similarly contributes to the asymmetries seen in the other two of the non-centered cuts. As we can see similar effects in the star-masked image of MBH (their Figure 2), and as their data are in accord with ours, we are equally forced to the conclusion that their detection of a halo around NGC 5907 was an artifact caused by the same combination of ring light and unaccounted faint wings from their foreground stars that affects our data.

5. CONCLUSION

We have obtained very deep images of the edge-on galaxy NGC 5907 with two intermediate-band filters on the BATC system (cf. Fan et al. 1996), m_{6660} and m_{8020}. Via a detailed assessment of the sources of our errors, we show that our limiting magnitudes (where the observational error reaches 1 mag arcsec^{-2}) are 29.0 mag arcsec^{-2} in the 6660Å image (corresponding to 28.7 in R-band measures) and 28.0 mag arcsec^{-2} in the 8020Å image (close to the I-band system). This is over one magnitude fainter than previously published measurements, owing mostly to the much darker sky as seen in our intermediate-band filters.

We use a new method of sky subtraction that both can account for most of the foreground star contamination (by PSF-fitting the star profiles first, then subtracting the fit), and permits reasonable interpolation of sky under the galaxy region while also fitting the inherent lumpiness of the sky at low surface brightnesses (using interactive fits of bidirectional, low-order Legendre polynomials and heavy smoothing). Our use of diffuser-smoothed dome flats, already shown to give accurate photometric results over a wide range of stellar colors (Fan et al. 1996) are again shown to give reliable flatfields with these data. This is critical, as it can be easily shown (cf. Wild 1997) that the sky is not flat anywhere on degree size scales.

As first shown by Shang et al. (1998), we detail the evidence that NGC 5907 has an elliptical-shaped ring of emission around it, which mostly likely is the remnant of a dwarf spheroidal galaxy that has been tidally torn apart. Within errors of 0.3 – 0.4 mag arcsec^{-2}, we show that the R–I colors of the brighter part of this ring are consistent with the light coming from a moderately metal-poor old stellar population.

We investigate the surface brightness distribution perpendicular to the disk of NGC 5907 by taking the same cuts through the galaxy as MBH. We show that all of the faint, extended surface brightness we observe perpendicular to the disk of NGC 5907, and above an altitude of 5 kpc, is most likely due to contamination by ring light and by residual effects from foreground star contamination. The possibility of a face-on warp existing in NGC 5907, suggested by our HI observations, is too confused with foreground star contamination to permit us to prove or disprove its optical existence.

Our comparisons to the existing perpendicular profiles in the literature for NGC 5907 find us in substantial agreement, once predicted zero point differences are removed, with these data. Of particular note is that with the known zero point difference between our 6660Å filter and the R band removed, the our data and those of MBH are in excellent agreement.

As such, we find that previous claims by Sackett et al. and others that NGC 5907 has a faint halo to be an artifact due to a combination of two factors. One is the added light complications from the presence of a previously-unknown ring around the galaxy. The second factor is the unaccounted residual effects of the foreground star masking procedures for both our data and those of MBH at faint levels. The lack of a halo around NGC 5907 is evident directly from our deep images of this galaxy (Figures 2a and 6a), once one understands that the ring we detect has an average 6660Å surface brightness of 28th mag arcsec^{-2}.

We thank Jinyao Hu and Xiaowei Liu for comments and discussions, Elias Brinks for his help in obtaining the VLA data, Heather Morrsion for supplying us with the data of MBH, and the referee for helpful comments. The research done with the BATC Survey is supported by the Chinese Academy of Sciences (CAS), the Chinese National Natural Science Foundation (CNNSF) and the Chinese State Committee of Sciences and Technology (CSCST). It is also supported in part by the U.S. National Science Foundation (NSF Grant INT-93-01805), by Arizona State University, the University of Arizona and Western Connecticut State University.

REFERENCES

Barnaby, D. & Thronson, H. A. 1992, AJ, 103, 41

Chen, J.-S. et al. 1999, in preparation

James, P. & Casali, M. M. 1996, Spectrum, March, 14

Fan, X.-H. et al. 1996, AJ, 112, 628

Lasker, B. M., et al., 1990, AJ, 99, 2019

Lequeux, J., Fort, B., Dantel-Fort, M., Cuillandre, J.-C. & Mellier, Y. 1996, A&A, 312, L1

Lequeux, J. et al. 1998, astro-ph/9804109

Morrison, H. L., Boroson, T. A., & Harding, P. 1994, AJ, 108, 1191 [MBH]

Oke, J. B. & Gunn, J. E., 1983, ApJ, 266, 713

Peterson, R. C., Dalle Ore, C. M. & Kurucz, R. L. 1993, ApJ, 404, 333

Rudy, R. J., Woodward. C. E., Hodge, T., Fairfield, S. W. & Harker, D. E. 1997, Nature, 387, 159

Sackett, P. D., Morrison, H. L., Harding, P., & Boroson, T. A. 1994, Nature, 370, 441

Sancisi, R. 1976, A&A, 53, 159

Sancisi, R. 1993, private communication

Sasaki, T. 1987, PASJ, 39, 849

Shang, Z.-H. et al. 1998, ApJL, accepted

Skurtskie, M. F., Shure, M. A. & Beckwith, S. 1985, ApJ, 299, 303

Stetson, P. B. 1987, PASP, 99, 191

Stetson, P. B. 1990, PASP, 102, 932

Tonry, J. & Schneider, D. P. 1988, AJ, 96, 807

Tonry, J. L., Ajhar, E. A., & Luppino, G. A. 1990, AJ, 100, 1416

van der Kruit, P. C. 1979, A&AS, 38, 15

van der Kruit, P. C. & Searle, L., 1981, A&AS, 95, 105

Wild, W. J. 1997, PASP, 109, 1269

Fig. 1.— The mean values of sky level, flux and FWHM for 20 comparison stars found in common on all the frames in 6660Å filter. The data of adjacent observations are displayed with different symbols. With these parameters we selected out images with high signal-to-noise ratio so that we can get data as accurate as possible.

Fig. 2a.— The 6660Å, $26^{\rm h}20^{\rm m}$ combined deep image of NGC5907. The central square shows the area used in photometry, which is 1000×1000 pixels. The ring around NGC 5907 can be seen faintly in this image; its mean surface brightness is 28th 6660Å mag arcsec^{-2}.

Fig. 2b.— The 8020Å, $16^{\rm h}40^{\rm m}$ combined image of NGC5907. Note the ring is of too faint a surface brightness to be seen in this image.

Fig. 3.— Four examples of subtracting and masking stars and galaxies. (a) A saturated bright star. This PSF cannot be subtracted by DAOPHOT. Its wing extends so far that the mask radius is larger than 130 pixels. Another saturated star is found near this one. Their mask circles exclude most contamination of their extended wings. (b) An unsaturated bright star. The residuals after the PSF is fit shows that the central pixels have large fluctuations around the sky level and the residual wing of its PSF is still partly visible. The mask radius used is 21 pixels. (c) A star of moderate brightness. The residuals after PSF is fit show significantly smaller variation in its center than for the bright star, and the PSF wings for this star are smaller as well. The mask radius used is 10 pixels. (d) A faint galaxy. The PSF for a galaxy is much gradual than that of stars, such that it can not be subtracted properly by DAOPHOT using a stellar PSF. The mask radius used is 9 pixels, while a star with the same brightness needs a mask radius of only 5 pixels or less.

Fig. 4.— The final mask that will be applied to the 6660Å image to account for foreground stars and background galaxies and a circle region around NGC 5907. The central circle indicates the region in which all pixels around NGC 5907 are masked; the curved area around this circle masks the ring we found around this galaxy. Separately, for profile determinations the dust lane of NGC 5907 is also masked. The mask radii of most faint stars are too small in size and low in contrast to be clearly displayed in this image.

Fig. 5.— The four steps of fitting background. (a) Fit the image row by row with Legendre polynomials of order 3 or less. (b) Fit the image column by column in the same way. (c) Take the average of (a) and (b). (d) Smooth (c) with a Gaussian function. It can be found that the final fitted background is too complicated to be expressed by any 2-D analytical function. The net results of the fit underneat the galaxy region are shown in the slices in Figures 7 and 8.

Fig. 6a.— The background–subtracted image in 6660Å. The ring around the galaxy is very clear. It is a near-perfect, but not complete ellipse, with a major axis of $13.7'$, minor axis of $7.2'$ and eccentricity $e = 0.84$ (cf. Shang et al. 1998). The major axis size is 44 kpc at a predicted distance of 11 Mpc (assuming $H_0 = 75$ km s^{-1} Mpc^{-1}). The area within the rectangle marked in the image was measured to determine the average surface brightness of the brightest area of the ring in 6660Å and 8020Å, so that we can get color index of the ring with reasonable accuracy. A schematic figure is inserted in bottom-right corner of the image to show the relative position of the ring and the galaxy. The solid lines with labels indicate the cuts along which surface photometry of the galaxy halo is done. These cuts are the same as that of Sackett et al. (1994) and MBH. The dashed lines show the centers of the slices made to check effect of background-subtraction. Note the extent to which foreground stars exist to affect the surface brightness distributions we can obtain in the MBH cuts.

Fig. 6b.— The background-subtracted image in 8020Å.

Fig. 7.— Four slices in the background–subtracted 6660Å image to show the accuracy of background fitting and local surface brightness of the ring feature. The positions of the center of each slice relative to the galaxy and ring are repreented in Fig. 6a by the dashed lines. Each slice is averaged over 31 lines of the image, and only non-masked pixels are averaged. In the case that all 31 points are masked, a zero value is assigned. Also shown are a straight line indicating the zero level. Note also the small, but still apparent, residual effect of our star subtraction/masking procedure, a product of the compromise made in the star masking procedure. The lower part of each panel (i.e., below the zero lines) shows the residuals of subtracted sky background for each slice. The upper line in each panel shows the residuals produced by our sky fitting procedure, while the lower line shows that produced by normal two-dimensional function fitting. They are shifted down by 110 ADU and 150 ADU seperately for ease of display. One can compare them and easily find that our procedure produce smaller residuals. The arrows in the three panels show the positions where the slices cross the ring.

Fig. 8.— The slices in the background–subtracted 8020Å image, shown in the same format as in Figure 7.

Fig. 9.— The stellar warp of NGC5907 measured in two bands. The circles are from 6660Å image and the squares are from 8020Å image. The x axis is along the galaxy plane, which is determined by fitting the symmetry axis of the galaxy. The stellar warp is obvious even in the cut nearest the galaxy center.

Fig. 10.— The surface brightness profiles in the 6660Å passband for the seven MBH–consistent cuts perpendicular to the galaxy plane. Each panel corresponds to one cut shown in Fig. 6a and the separate measurements of the two sides of the galaxy plane are shown. The data of NE and SW side of the galaxy plane are denoted by squares and triangles, respectively. The open symbols denote the points affected by the ring. Central regions of the galaxy are excluded due to star and dust masking. The asymmetries at faint surface brightnesses that exist in these cuts are discussed in the text.

Fig. 11.— The surface brightness profiles in 8020Å.

Fig. 12.— Comparison of our 6660Å data with that of MBH, with a zero point shift of 0.3 mag applied to the MBH data to account for the different passbands used. The circles are the data of MBH that were sent to us by Dr. Morrison, which go fainter than those published by MBH in their actual paper. The solid circles are the reliable data claimed by them and published in Sackett et al. 1994, while the open circles (fainter than 27 mag arcsec^{-2}) were not published. The other symbols have the same meaning as Fig.10. Note the general good agreement between our data and those of MBH (save for cuts A and C2) even at surface brightnesses fainter than 27th mag arcsec^{-2}.

Fig. 13.— Comparison of our 8020Å data with infrared data from Rudy et al. (J and K) and Lequeux et al. (I), with zero point applied to the published data as discussed in the text. Note the general good agreement among the different passbands, with their mutual errors, except for the "bump" seen in the data of Rudy et al. but not in the other data sets.

Fig. 14.— The m_{6660}-m_{8020} color profiles of NGC5907. Measurable color gradients become bluer with distance from the galaxy midplane in all cuts except D2, where the color gradient actually becomes redder with distance from the midplane. The meaning of the symbols is the same as they in Fig. 10 and Fig. 11. It is apparent that the errors in the colors preclude any meaningful measurement of color gradient outside of 4 kpc from the plane of this galaxy.

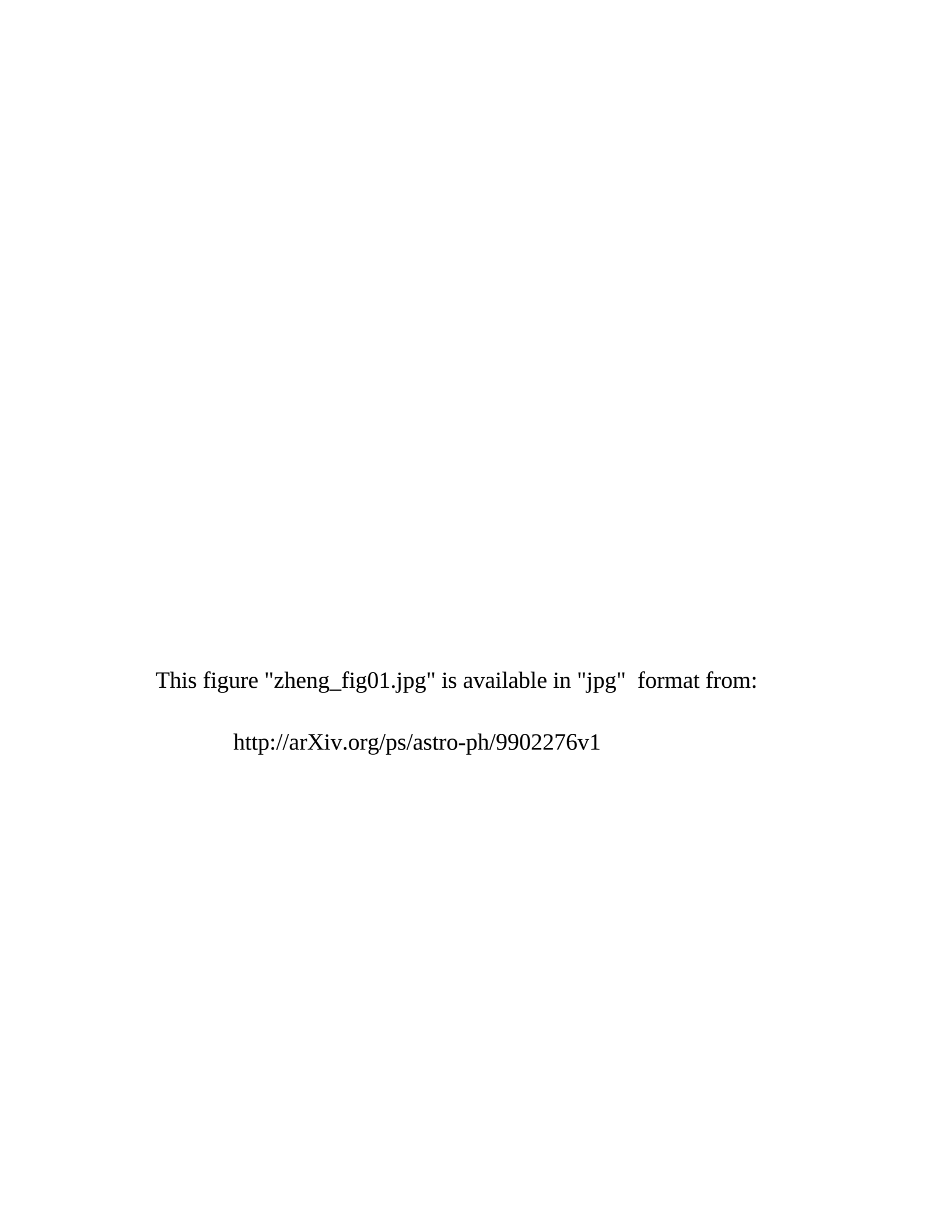
This figure "zheng_fig01.jpg" is available in "jpg" format from:
http://arXiv.org/ps/astro-ph/9902276v1

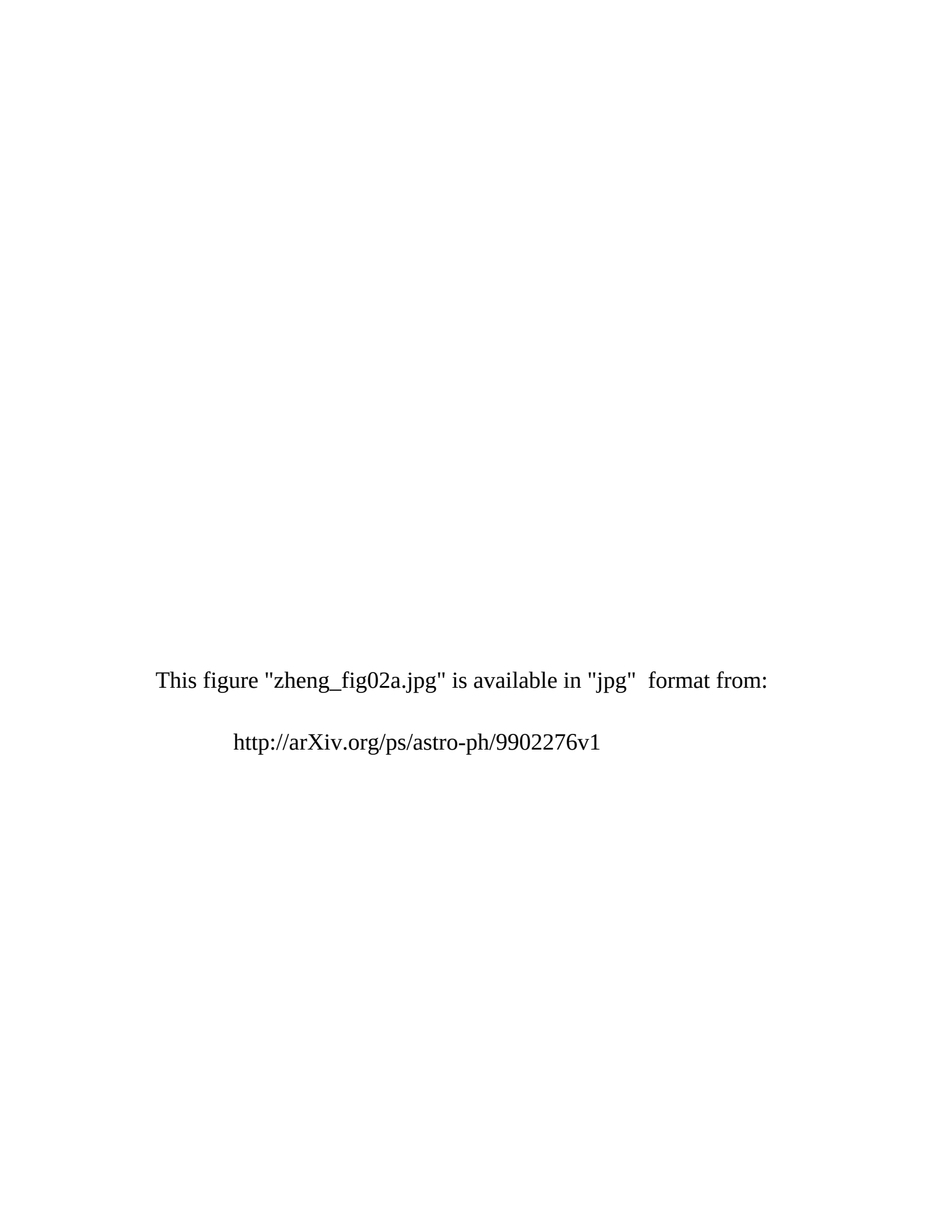
This figure "zheng_fig02a.jpg" is available in "jpg" format from:
http://arXiv.org/ps/astro-ph/9902276v1


This figure "zheng_fig02b.jpg" is available in "jpg" format from:
http://arXiv.org/ps/astro-ph/9902276v1

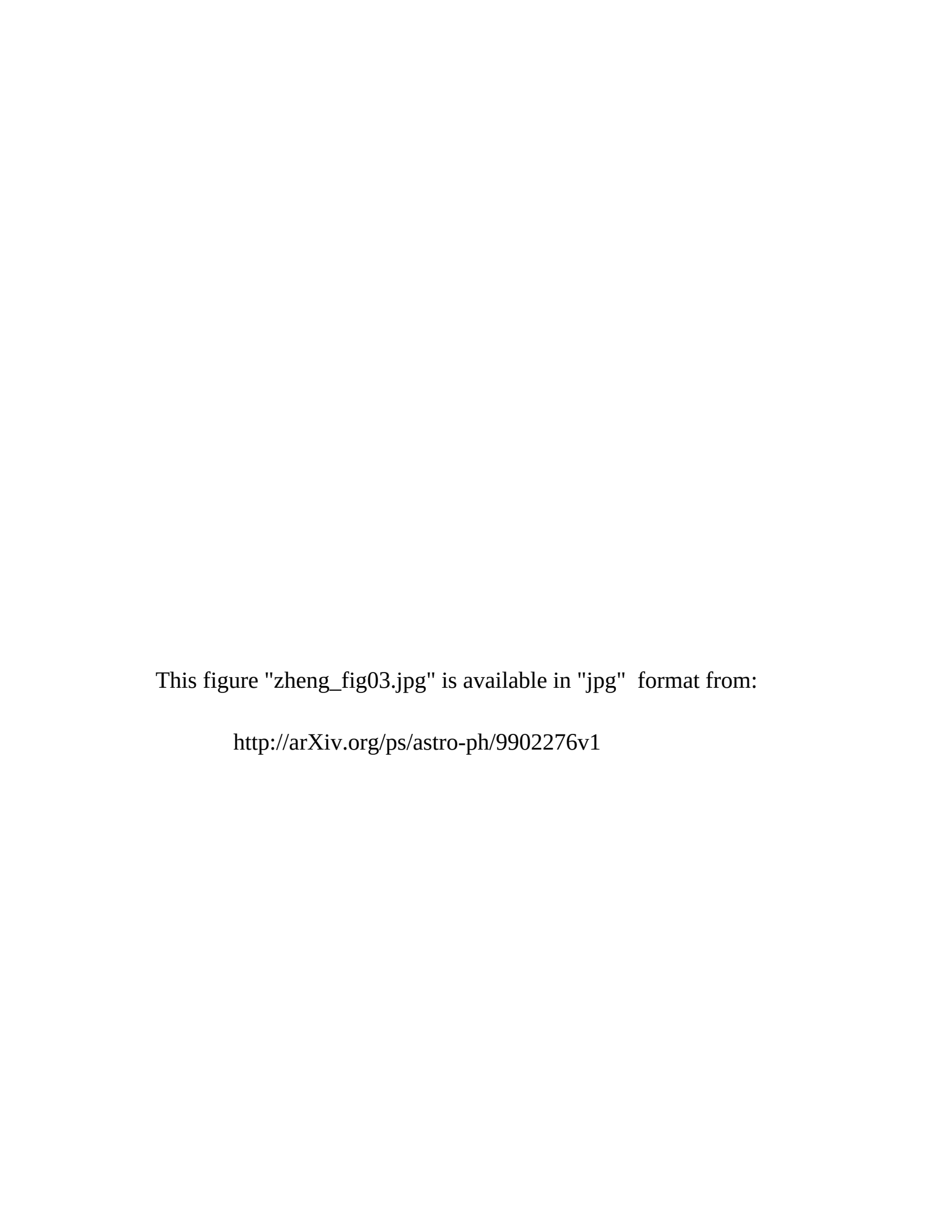
This figure "zheng_fig03.jpg" is available in "jpg" format from:
http://arXiv.org/ps/astro-ph/9902276v1

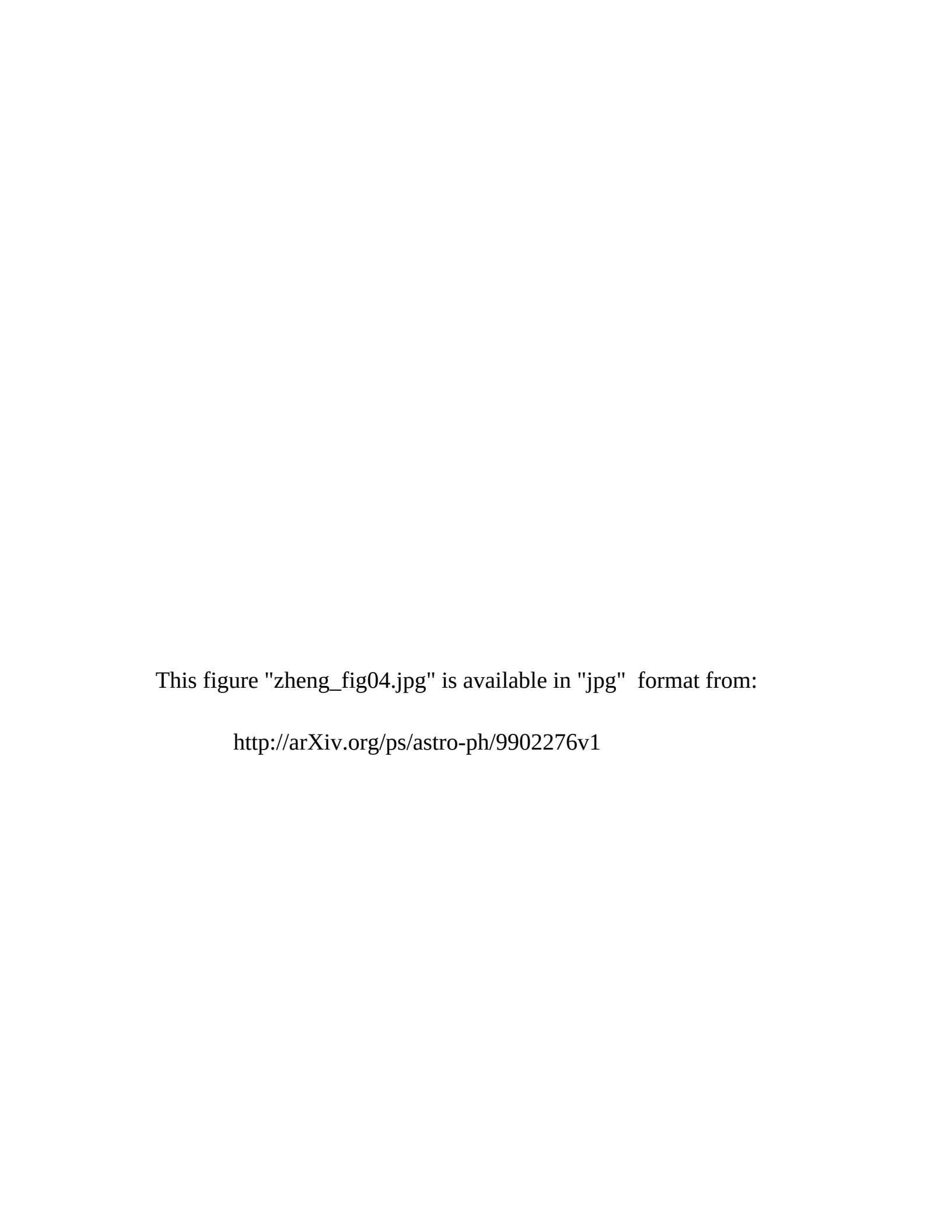
This figure "zheng_fig04.jpg" is available in "jpg" format from:
http://arXiv.org/ps/astro-ph/9902276v1

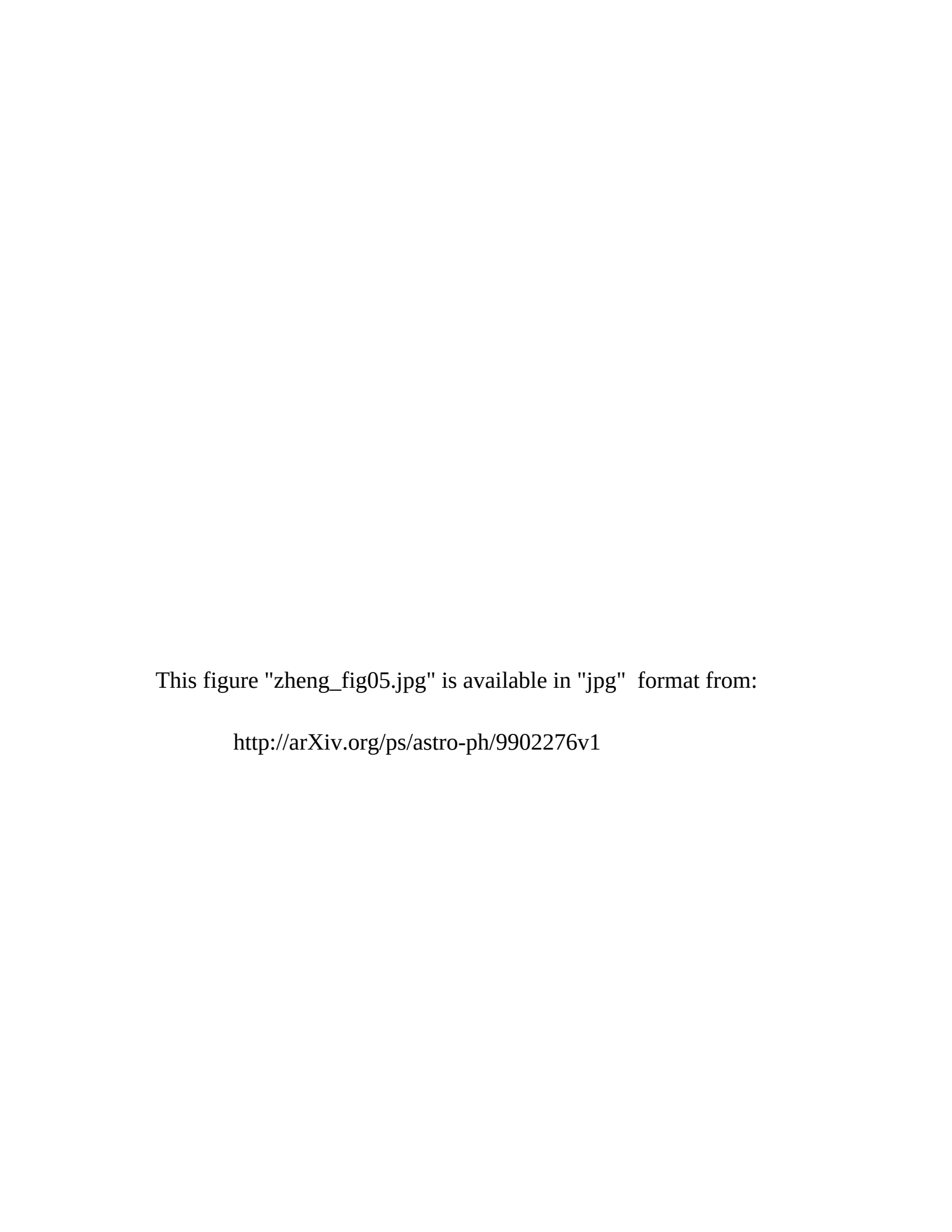
This figure "zheng_fig05.jpg" is available in "jpg" format from:
http://arXiv.org/ps/astro-ph/9902276v1

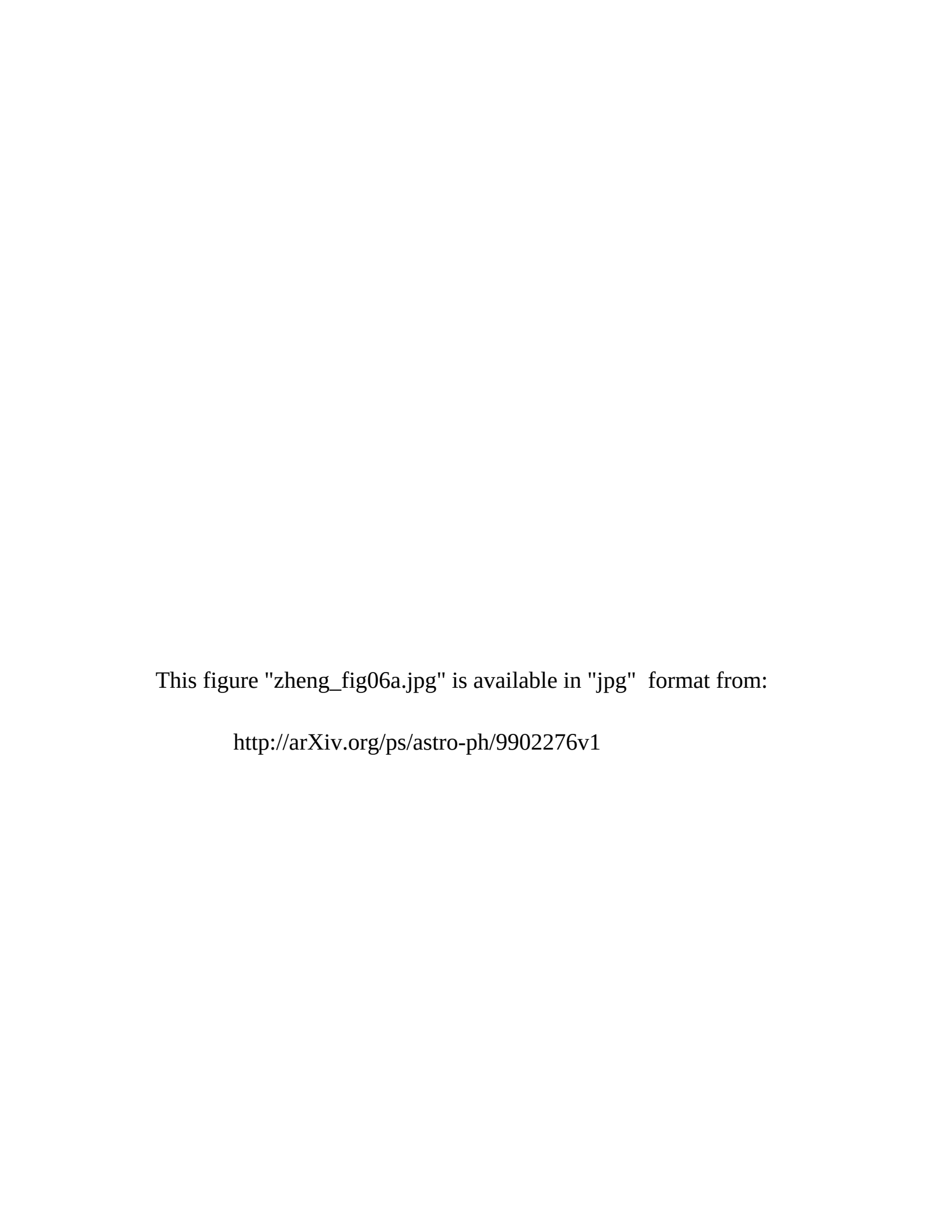
This figure "zheng_fig06a.jpg" is available in "jpg" format from:
http://arXiv.org/ps/astro-ph/9902276v1


This figure "zheng_fig06b.jpg" is available in "jpg" format from:
http://arXiv.org/ps/astro-ph/9902276v1

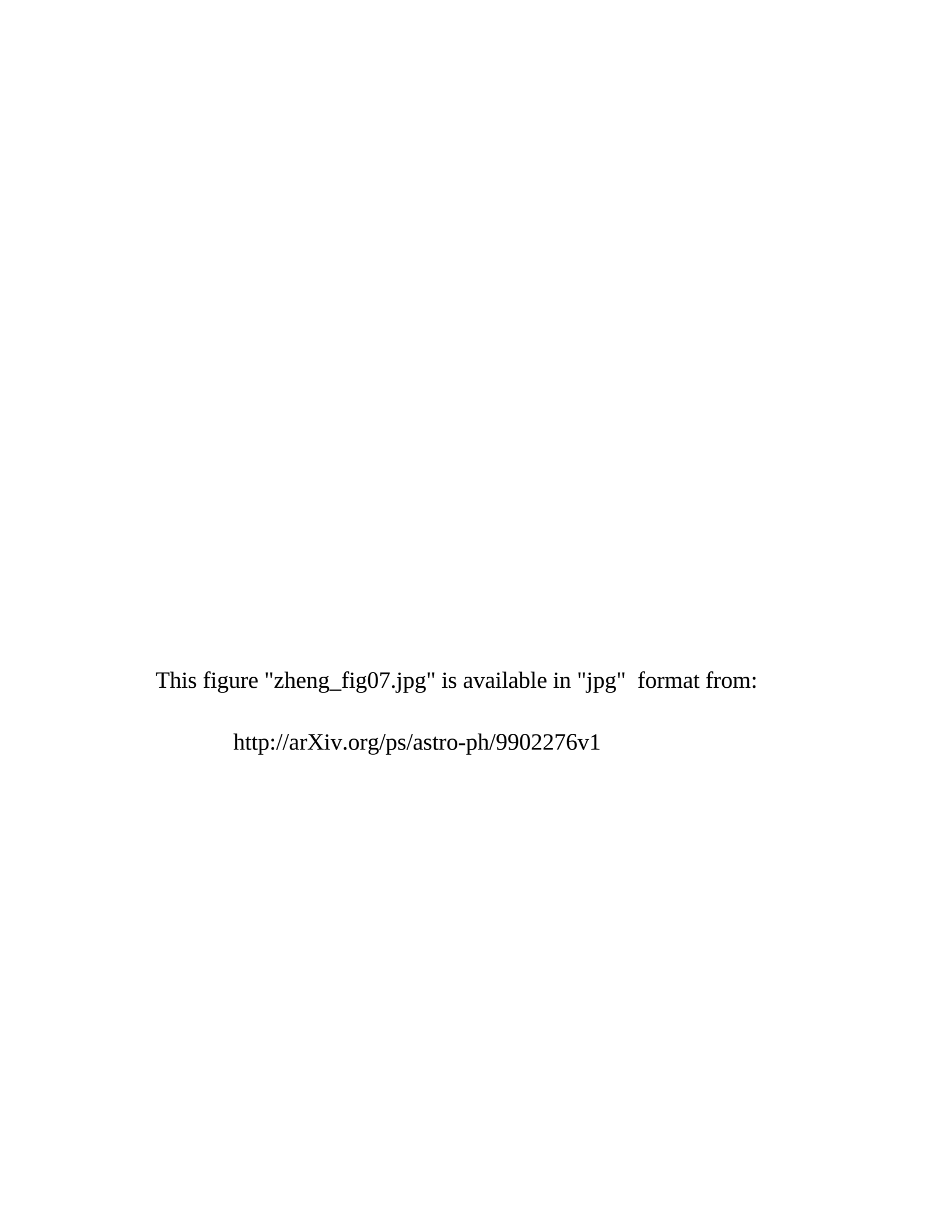
This figure "zheng_fig07.jpg" is available in "jpg" format from:
http://arXiv.org/ps/astro-ph/9902276v1

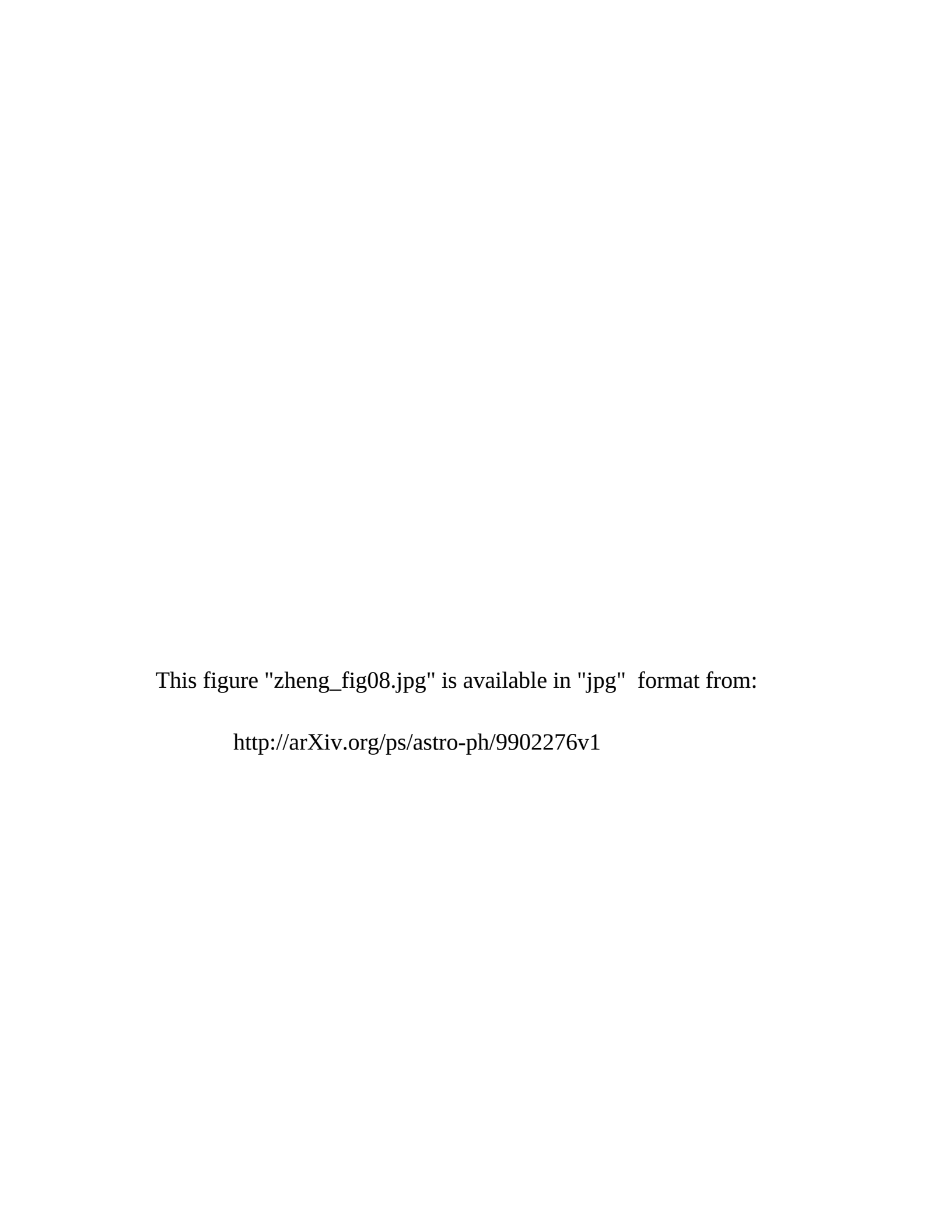
This figure "zheng_fig08.jpg" is available in "jpg" format from:
http://arXiv.org/ps/astro-ph/9902276v1

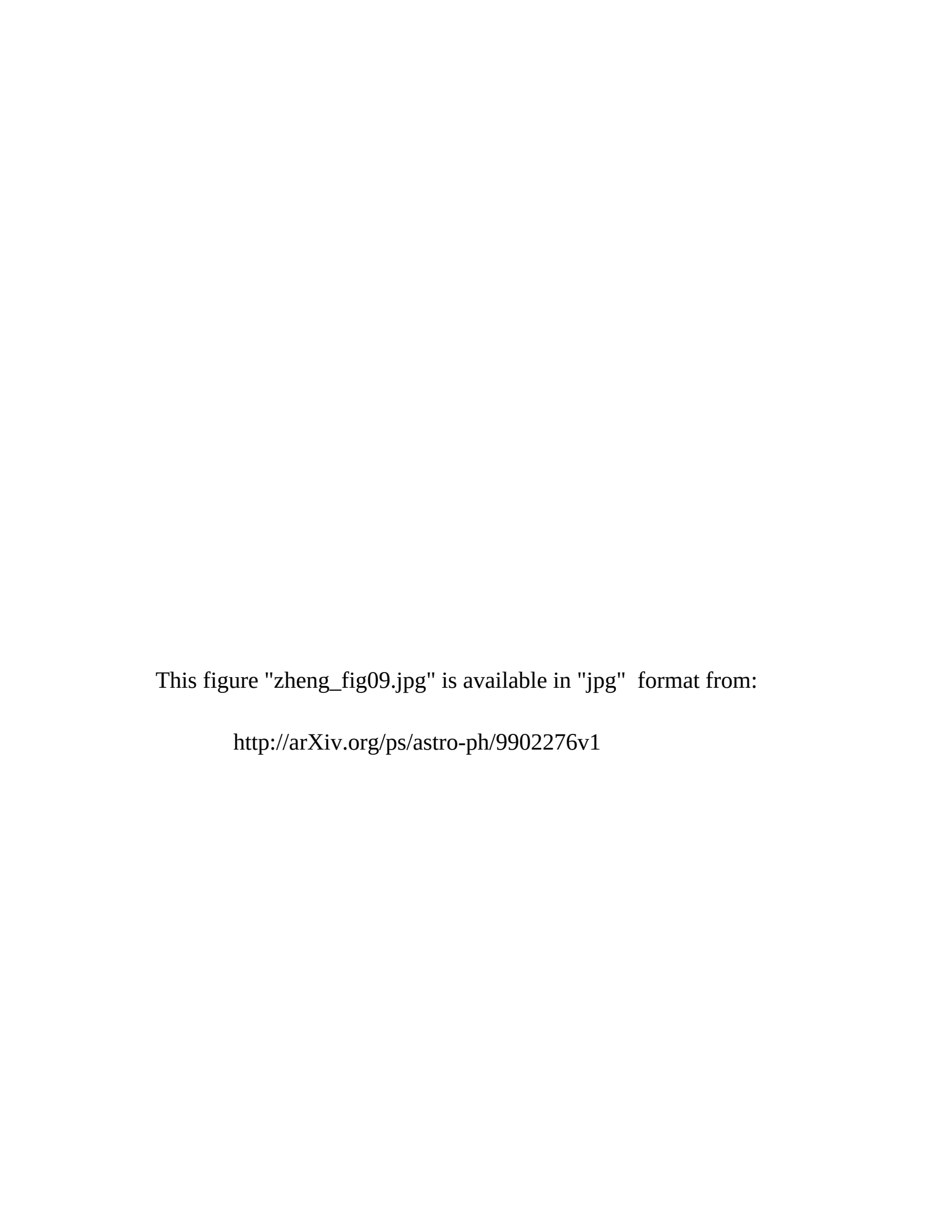
This figure "zheng_fig09.jpg" is available in "jpg" format from:
http://arXiv.org/ps/astro-ph/9902276v1

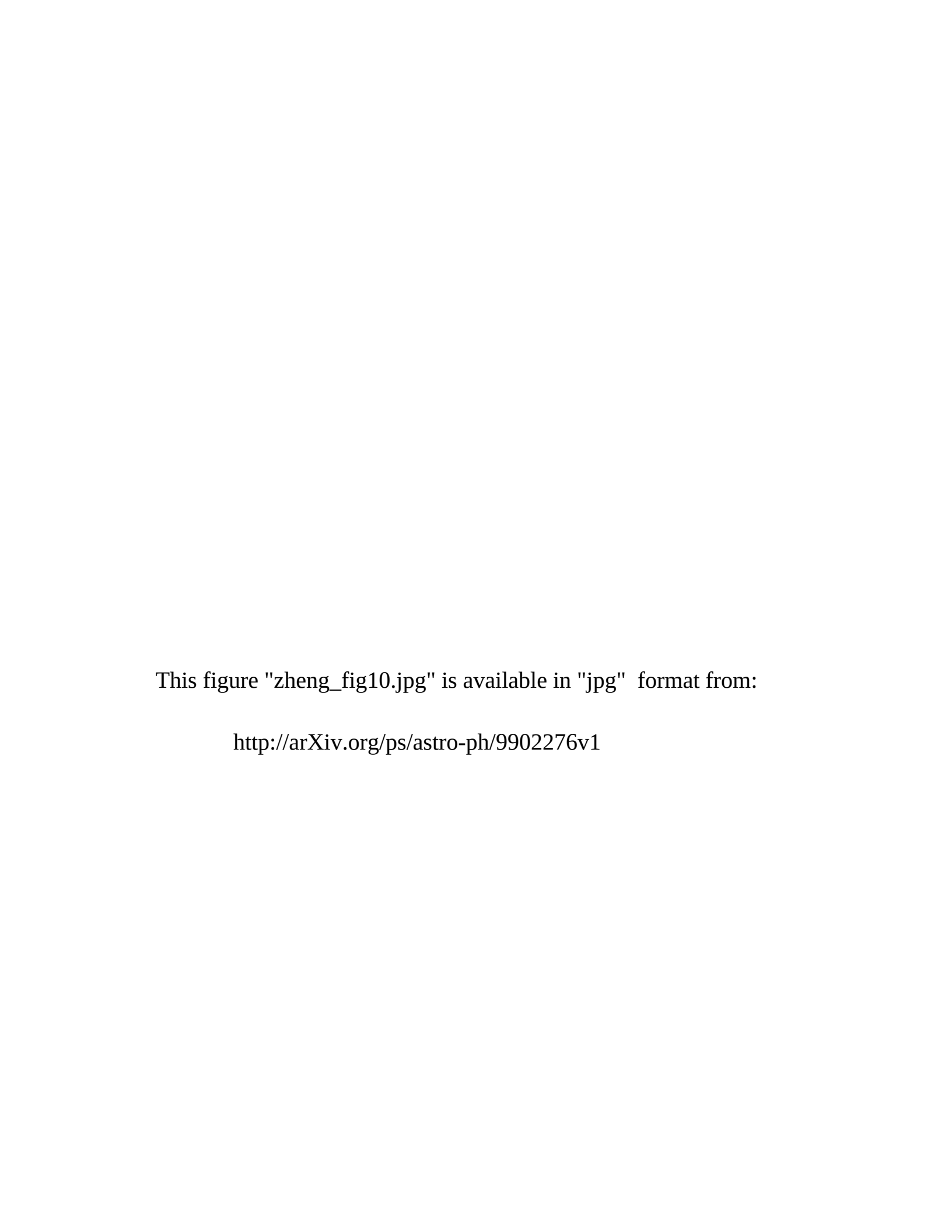
This figure "zheng_fig10.jpg" is available in "jpg" format from:
http://arXiv.org/ps/astro-ph/9902276v1

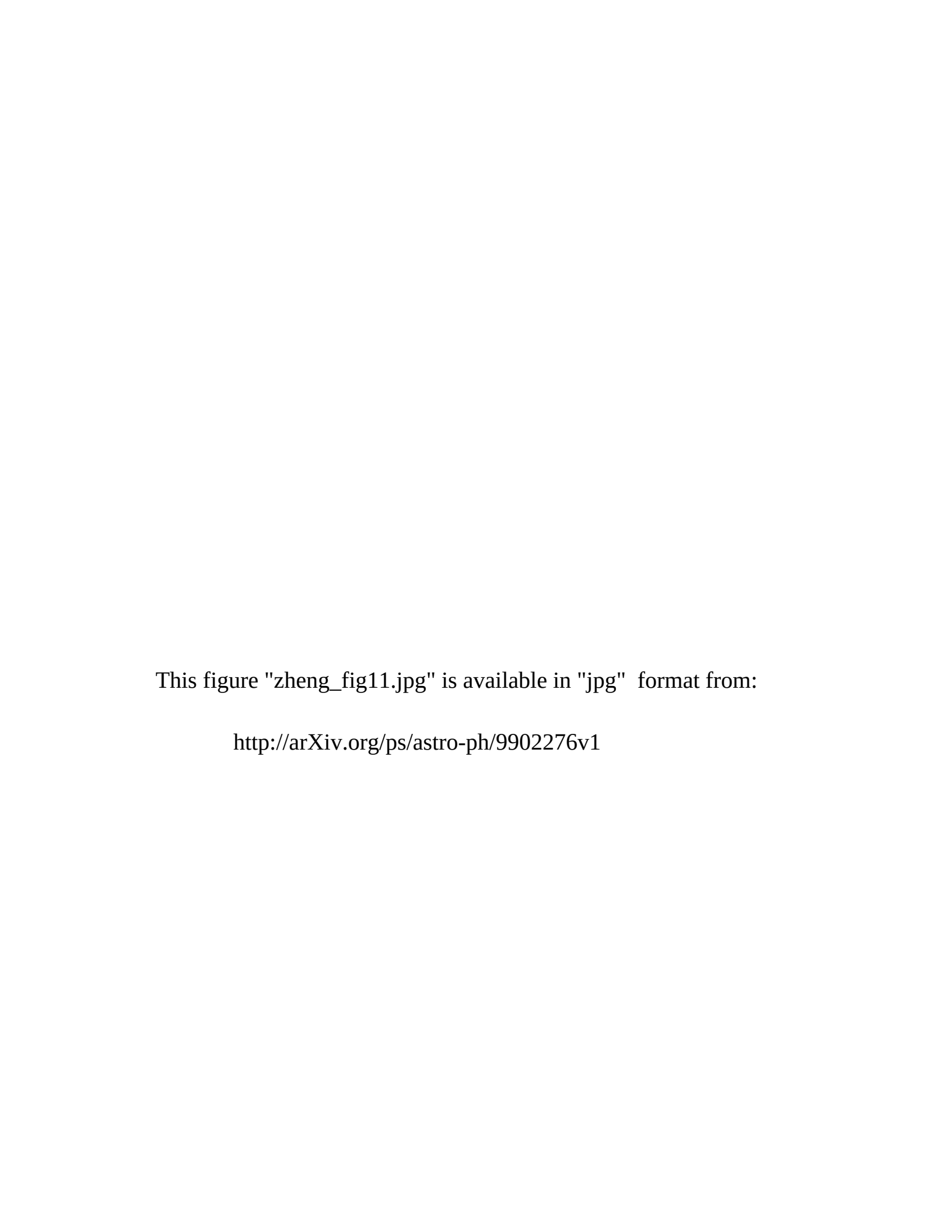
This figure "zheng_fig11.jpg" is available in "jpg" format from:
http://arXiv.org/ps/astro-ph/9902276v1

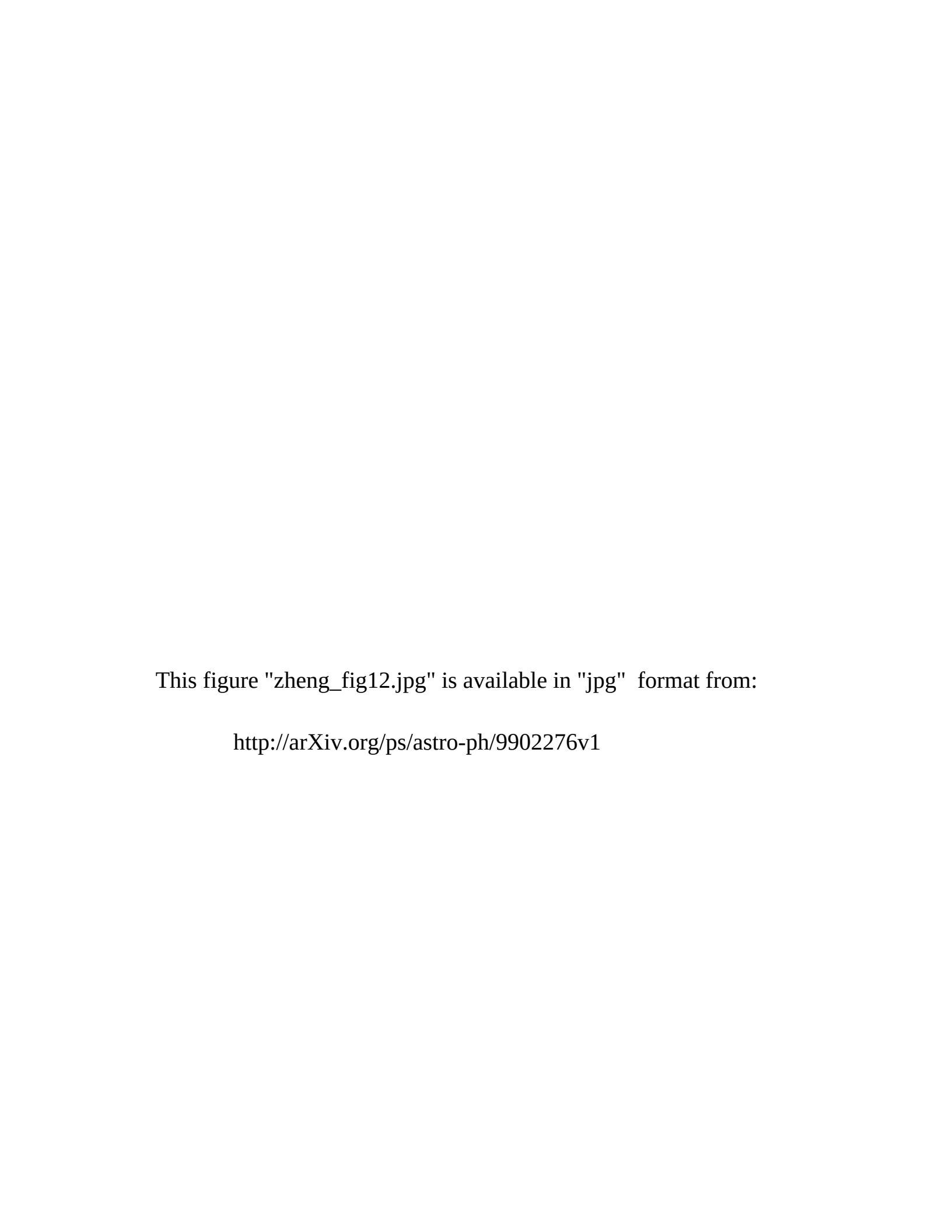
This figure "zheng_fig12.jpg" is available in "jpg" format from:
http://arXiv.org/ps/astro-ph/9902276v1

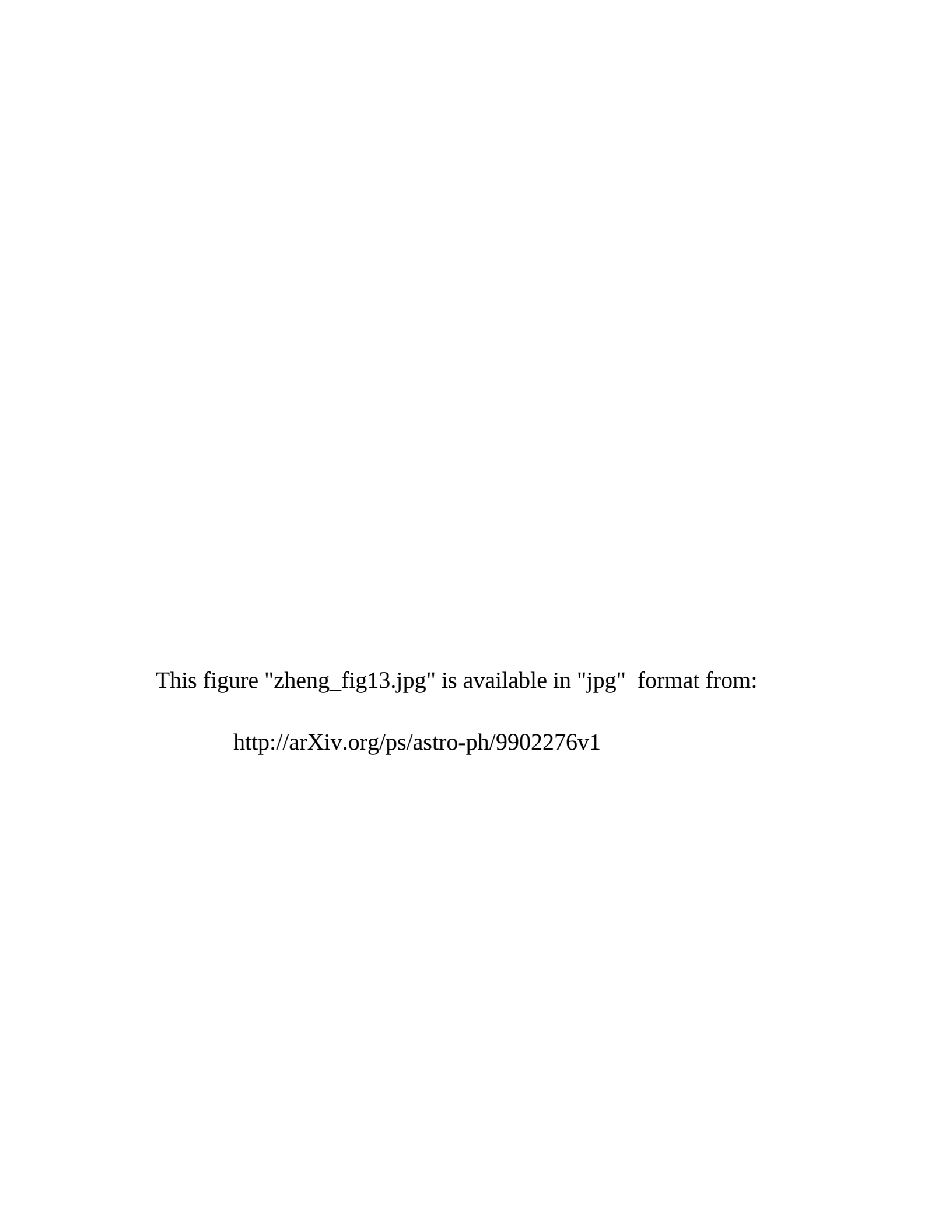
This figure "zheng_fig13.jpg" is available in "jpg" format from:
http://arXiv.org/ps/astro-ph/9902276v1

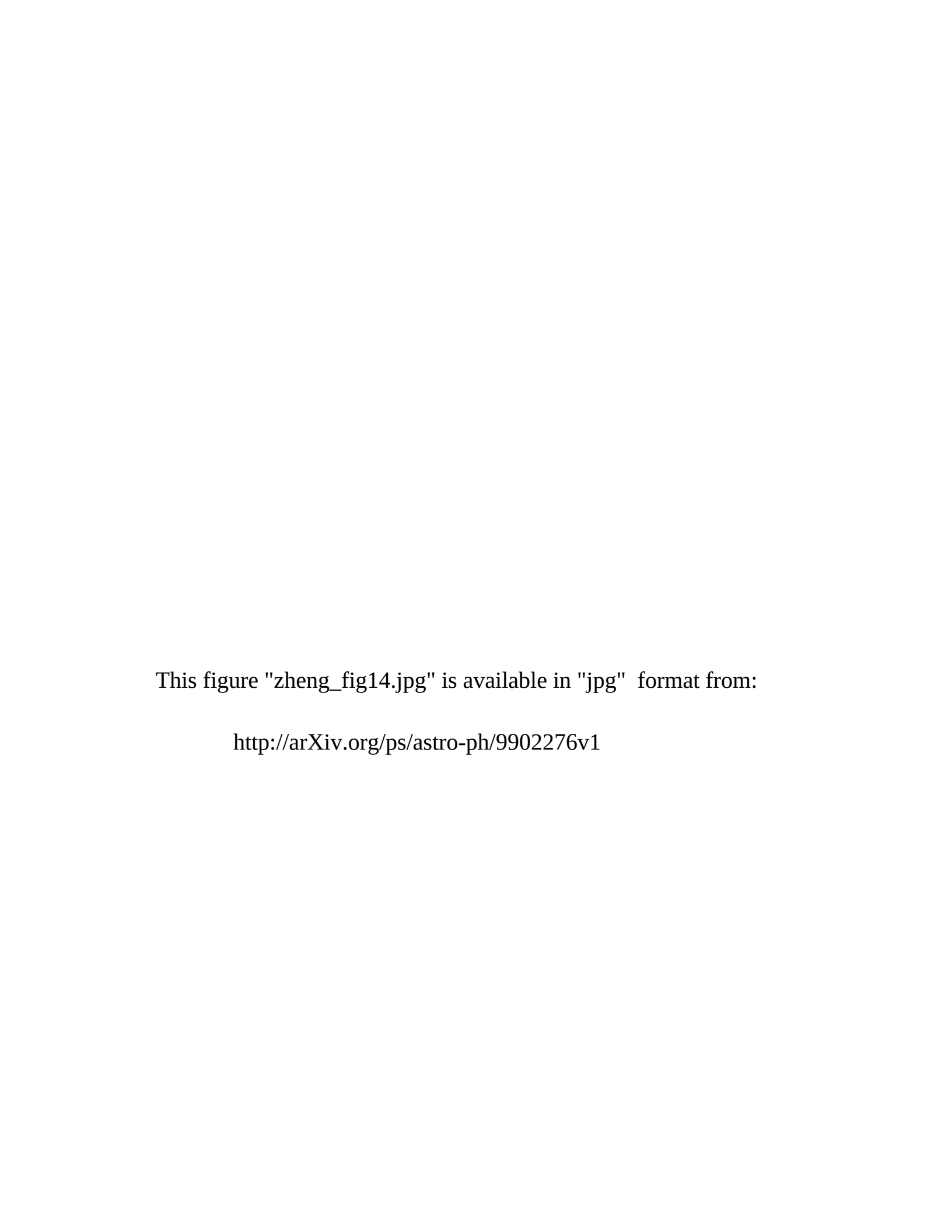
This figure "zheng_fig14.jpg" is available in "jpg" format from:
http://arXiv.org/ps/astro-ph/9902276v1

TABLE 1. Log of 6660Å images used

Image name[a]	Date DD/MM/YY	Time UT	Exposure (second)	Flux[b] (ADU)	Sky level[c] (ADU)	Seeing[d] FWHM(pixel)
p0119803N014i019	26/03/95	18:07:21	1200	45688.32	391.19	2.08
p0119803N014i020	26/03/95	18:29:40	1200	45763.04	395.91	2.21
p0119803N014i021	26/03/95	18:51:57	1200	45903.98	399.51	2.23
p0119803N014i023	26/03/95	19:36:53	1200	46019.57	442.44	2.05
p0119803N014i024	26/03/95	19:59:28	1200	44634.13	481.58	2.39
p0129807N014i003	30/03/95	17:54:08	1200	43494.19	426.55	1.95
p0129807N014i005	30/03/95	18:38:37	1200	44200.91	427.85	1.95
p0129807N014i007	30/03/95	19:25:27	1200	43784.82	467.94	2.05
p0129808N014i009	31/03/95	16:48:28	1200	40461.00	458.07	2.14
p0129808N014i010	31/03/95	17:12:47	1200	39162.06	439.75	2.20
p0129808N014i011	31/03/95	17:37:00	1200	40732.67	440.08	1.98
p0129808N014i013	31/03/95	18:23:59	1200	41581.18	409.74	1.94
p0129808N014i014	31/03/95	18:46:20	1200	41918.14	409.81	2.07
p0129808N014i015	31/03/95	19:08:59	1200	42205.07	416.94	1.87
p0129808N014i016	31/03/95	19:31:40	1200	41838.50	421.53	2.44
p0129810N014i033	02/04/95	16:08:17	600	37385.97	442.13	1.90
p0129810N014i034	02/04/95	16:20:45	600	38249.45	426.84	1.80
p0129810N014i035	02/04/95	16:35:48	600	38808.16	421.85	1.88
p0129810N014i036	02/04/95	16:49:31	600	38612.60	414.41	2.30
p0129810N014i090	02/04/95	18:43:11	600	41381.23	405.56	2.07
p0129810N014i091	02/04/95	18:55:39	600	40778.88	409.80	2.17
p0129810N014i092	02/04/95	19:07:57	600	40927.23	420.08	2.10
p0129810N014i093	02/04/95	19:20:15	600	41159.31	423.30	2.12
p0129810N014i094	02/04/95	19:32:49	600	40996.85	424.98	2.07
p0129810N014i095	02/04/95	19:45:06	600	41282.66	434.43	1.93
p0129810N014i096	02/04/95	19:57:26	600	40685.38	447.11	2.07
p0129813N014i005	05/04/95	17:33:41	1200	41198.76	410.51	2.23
p0129813N014i006	05/04/95	17:56:09	1200	40817.11	396.47	2.29
p0129813N014i007	05/04/95	18:20:29	1200	42195.56	380.21	2.18
p0129813N014i008	05/04/95	18:42:52	1200	40453.31	374.80	2.36
p0129813N014i010	05/04/95	19:28:17	1200	40533.32	412.19	2.35
p0159832N014i011	24/04/95	16:25:51	1200	35953.96	450.15	3.33
p0159832N014i012	24/04/95	16:49:12	1200	35878.17	456.35	3.38
p0159832N014i013	24/04/95	17:16:16	1200	38954.00	466.10	2.89
p0159832N014i014	24/04/95	17:39:47	1200	40301.73	517.22	2.58
p0159832N014i015	24/04/95	18:03:18	1200	41408.85	574.39	2.33
p0159840N014i003	02/05/95	16:24:05	1200	35074.59	479.29	1.75
p0159840N014i004	02/05/95	16:49:06	1200	37000.46	487.52	1.82
p0159840N014i005	02/05/95	17:14:12	1200	37660.10	519.02	1.84
p0159840N014i006	02/05/95	17:39:27	1200	38818.73	530.52	2.17
p0159840N014i007	02/05/95	18:07:31	1200	39185.15	523.33	2.25
p0159840N014i008	02/05/95	18:32:47	1200	39221.22	516.27	2.20
p0159840N014i009	02/05/95	18:56:33	1200	38255.55	519.34	2.42
p0159841N014i002	03/05/95	16:26:44	1200	33645.56	507.71	1.65
p0159841N014i003	03/05/95	16:50:30	1200	37463.91	470.97	1.64
p0159841N014i004	03/05/95	17:13:39	1200	38350.46	470.50	2.01
p0159841N014i005	03/05/95	17:37:20	1200	38007.07	460.79	1.86
p0159841N014i006	03/05/95	18:01:55	1200	38629.03	449.87	1.72

TABLE 1. (continued)

Image name[a]	Date DD/MM/YY	Time UT	Exposure (second)	Flux[b] (ADU)	Sky level[c] (ADU)	Seeing[d] FWHM(pixel)
p0159841N014i007	03/05/95	18:25:25	1200	38639.90	451.50	1.74
p0159841N014i008	03/05/95	18:50:47	1200	38605.21	477.84	1.76
p0169843N014i005	05/05/95	15:57:59	1200	34936.81	455.66	1.85
p0169843N014i006	05/05/95	16:21:19	1200	34240.71	448.46	1.89
p0169843N014i007	05/05/95	16:47:35	1200	33895.24	464.00	1.85
p0169843N014i008	05/05/95	17:11:23	1200	33179.18	458.11	1.91
p0169843N014i009	05/05/95	17:34:57	1200	32687.67	470.84	1.91
p0169843N014i010	05/05/95	17:58:08	1200	32377.79	481.40	1.90
p0169843N014i011	05/05/95	18:27:31	1200	32727.70	502.62	1.77
p0169843N014i012	05/05/95	18:53:45	1200	32214.26	547.08	1.74
p0169844N014i015	06/05/95	17:40:14	1200	35947.07	533.51	1.87
p0169844N014i016	06/05/95	18:03:27	1200	35808.12	521.69	1.88
p0169844N014i017	06/05/95	18:26:38	1200	34774.71	546.38	1.92
p0169844N014i018	06/05/95	18:49:34	1200	33989.09	546.47	2.00
p0179860N014i000	22/05/95	14:58:24	1200	39589.11	515.46	2.66
p0179860N014i001	22/05/95	15:22:14	1200	38286.74	528.31	2.72
p0179860N014i002	22/05/95	15:46:07	1200	38195.22	520.04	2.65
p0179860N014i003	22/05/95	16:10:04	1200	37075.36	538.74	2.85
p0179860N014i004	22/05/95	16:35:15	1200	36371.84	562.57	2.87
p0179860N014i005	22/05/95	16:58:32	1200	34934.22	611.09	2.86
p0179862N014i009	24/05/95	16:36:55	1200	40573.72	458.35	1.98
p0179862N014i010	24/05/95	16:59:54	1200	40855.74	476.34	2.05
p0179862N014i011	24/05/95	17:22:40	1200	39471.87	540.44	2.23
p0179863N014i008	25/05/95	16:00:59	1200	42368.73	497.11	2.28
p0179863N014i009	25/05/95	16:23:13	1200	42437.13	511.08	2.14
p0179863N014i010	25/05/95	16:45:56	1200	42616.05	513.07	2.15
p0179863N014i012	25/05/95	17:30:51	1200	42919.03	523.20	2.16
p0179863N014i013	25/05/95	17:53:47	1200	42156.86	577.28	2.36
p0189873N014i007	04/06/95	15:24:25	1200	39912.96	502.76	2.13
p0189873N014i008	04/06/95	15:48:01	1200	40254.62	492.77	2.21
p0189873N014i009	04/06/95	16:10:39	1200	39109.38	505.35	2.36
p0189873N014i010	04/06/95	16:45:00	1200	38815.32	493.66	2.08
p0189873N014i011	04/06/95	17:07:40	1200	38853.51	492.20	2.09
p0209896N014i001	27/06/95	14:13:54	1200	40678.32	488.30	1.92
p0209896N014i002	27/06/95	14:38:33	1200	40598.48	499.05	1.71
p0209896N014i004	27/06/95	15:30:07	1200	40878.30	488.96	1.80

[a]The image name is organized as following sequence: prrrjjjjoooofsss
p = PIPELINE–I processed data
rrr = run number
jjjj = Julian date, only the last four digits are used
oooo = object number, NGC 5907 has two numbers: T514 and N014
f = filter used (i=6660Å, m=8020Å)
sss = observation sequence of given night
[b]Mean flux of the 20 comparison stars, normalized to 20m integration
[c]Mean near-field sky level for the 20 comparison stars, normalized to 20m integration
[d]Mean FWHM of the 20 comparison stars

TABLE 2. Log of 8020Å images used

Image name	Date DD/MM/YY	Time UT	Exposure (second)	Flux (ADU)	Sky level (ADU)	Seeing FWHM(pixel)
p0330135N014m039	21/02/96	19:02:58	1200	27634.88	506.71	2.09
p0330135N014m040	21/02/96	19:26:01	1200	27828.17	474.49	2.15
p0330135N014m041	21/02/96	19:48:33	1200	27768.68	453.67	2.03
p0330135N014m042	21/02/96	20:11:05	1200	27738.37	421.46	1.96
p0330135N014m043	21/02/96	20:33:50	1200	28107.29	395.21	1.97
p0330136N014m036	22/02/96	17:17:53	1200	27405.63	436.15	1.91
p0330136N014m037	22/02/96	17:41:21	1200	27723.22	454.58	1.90
p0330136N014m038	22/02/96	18:03:50	1200	27836.49	462.55	1.94
p0330136N014m039	22/02/96	18:26:24	1200	27933.66	439.44	1.92
p0330136N014m040	22/02/96	18:49:04	1200	27979.31	405.05	1.88
p0330136N014m041	22/02/96	19:11:39	1200	28081.59	414.47	1.90
p0330136N014m042	22/02/96	19:34:13	1200	28007.59	393.42	1.93
p0330136N014m043	22/02/96	19:56:38	1200	28007.20	383.90	1.92
p0330136N014m044	22/02/96	20:19:11	1200	28133.33	415.54	2.03
p0330136N014m045	22/02/96	20:41:35	1200	28087.49	402.87	2.17
p0330141T534m038	27/02/96	19:07:08	1200	24137.61	550.05	2.38
p0330141T534m039	27/02/96	19:29:47	1200	24496.86	589.32	2.26
p0330141T534m040	27/02/96	19:52:35	1200	24779.54	623.50	2.26
p0330141T534m041	27/02/96	20:15:21	1200	24840.06	671.74	2.23
p0330141T534m042	27/02/96	20:38:05	1200	24996.80	654.99	2.29
p0340153N014m035	10/03/96	18:32:29	1200	26708.87	749.01	2.30
p0340153N014m036	10/03/96	18:55:00	1200	26668.87	703.19	2.29
p0340153N014m037	10/03/96	19:17:42	1200	26710.86	683.35	2.57
p0340153N014m038	10/03/96	19:40:54	1200	26759.61	749.38	2.39
p0340153N014m039	10/03/96	20:03:40	1200	26791.77	764.89	2.23
p0340153N014m040	10/03/96	20:26:10	1200	26821.89	778.71	2.16
p0340157T534m042	14/03/96	17:52:54	1200	22775.84	520.57	2.40
p0340157T534m043	14/03/96	18:15:20	1200	23111.24	544.43	2.43
p0340157T534m044	14/03/96	18:37:57	1200	22794.46	560.05	2.46
p0360190N014m002	16/04/96	16:33:07	1200	31314.58	438.65	2.42
p0360190N014m003	16/04/96	16:56:39	1200	31275.79	480.01	2.38
p0360190N014m004	16/04/96	17:20:21	1200	31147.07	484.32	2.48
p0360190N014m005	16/04/96	17:44:13	1200	31053.15	477.52	3.19
p0360190N014m006	16/04/96	18:08:19	1200	31111.32	482.44	3.11
p0360190N014m008	16/04/96	19:00:01	1200	30521.54	359.35	3.41
p0360190N014m009	16/04/96	19:23:44	1200	30067.63	420.39	2.41
p0360191N014m020	17/04/96	17:00:54	1200	29464.94	414.97	1.98
p0360191N014m021	17/04/96	17:24:51	1200	29541.54	353.81	2.38
p0360191N014m022	17/04/96	17:48:24	1200	29756.01	330.02	1.68
p0360191N014m023	17/04/96	18:13:53	1200	29926.16	312.84	1.70
p0360191N014m024	17/04/96	18:36:24	1200	30251.59	313.91	1.81
p0360191N014m025	17/04/96	18:59:09	1200	30290.93	335.49	1.84
p0360191N014m026	17/04/96	19:21:42	1200	30314.27	333.15	1.96
p0370192N014m024	18/04/96	16:49:22	1200	29078.35	581.85	1.89
p0370192N014m025	18/04/96	17:11:48	1200	29211.13	552.14	1.77
p0370192N014m026	18/04/96	17:34:31	1200	28949.63	516.00	1.67
p0370192N014m027	18/04/96	17:57:22	1200	29204.02	531.85	1.82
p0370192N014m028	18/04/96	18:21:37	1200	29693.29	572.58	1.99

TABLE 2. (continued)

Image name	Date DD/MM/YY	Time UT	Exposure (second)	Flux (ADU)	Sky level (ADU)	Seeing FWHM(pixel)
p0370192N014m029	18/04/96	18:44:10	1200	29669.82	545.97	1.84
p0370192N014m030	18/04/96	19:06:46	1200	28722.99	590.20	2.05

Notes to Table 2.

See notes to Table 1

TABLE 3. Parameters of the combined images

Filter	Total exposure times	Seeing[a] FWHM(pixel)	Sky level (mag/sq arcsec)	$\sigma_{\rm sky}$[b] (ADU)	Readout noise[c] (e^-)	Zero point[d] (1ADU/s)
6660Å	26^h10^m	2.3	21.26	105	110	19.08
8020Å	16^h40^m	2.5	19.91	85	85	17.79

[a]Mean FWHM of all the stars in the field.
[b]The standard error of sky background per pixel.
[c]Total readout noise introduced into the final combined images per pixel.
[d]Photometry zero point calibrated by measuring Oke–Gunn standard stars.

TABLE 4. Summary of limiting error sources in a 45×45 pixel bin in the 6660Å image

Source of variation	ADU	%
Reducible noise		
Readout noise	0.6	0.002
Photon statistics	2.1	0.006
Bias and Dark	0.02	0.00005
Flatfielding errors	0.08	0.0002
Surface brightness fluctuations	0.3	0.0008
Irreducible noise		
Large-scale FF errors	3.7	0.01
Systematic error of background subtraction	18.0	0.05
Total	23.9	0.06

TABLE 5. Perpendicular surface brightness profiles of NGC 5907 in the 6660Å and 8020Å images

distance (arcsec)	distance (kpc)	6660Å (mag/sq arcsec)	error(6660Å) (mag/sq arcsec)	8020Å (mag/sq arcsec)	error(8020Å) (mag/sq arcsec)
Cut A, $r = 0$ kpc					
-184.63•	-9.83	28.91	0.72	···	···
-180.35•	-9.60	28.91	0.72	···	···
-173.43•	-9.23	28.70	0.60	···	···
-165.56•	-8.81	28.52	0.51	···	···
-158.21•	-8.42	28.28	0.41	···	···
-151.28•	-8.05	28.19	0.38	27.81	0.91
-144.70•	-7.70	28.12	0.36	27.54	0.71
-138.54•	-7.37	27.96	0.31	27.24	0.54
-132.64•	-7.06	27.82	0.28	27.24	0.55
-127.00•	-6.76	27.69	0.25	26.95	0.42
-121.62•	-6.47	27.50	0.21	26.79	0.36
-116.49◇	-6.20	27.33	0.18	26.62	0.32
-111.53◇	-5.94	27.12	0.15	26.65	0.33
-102.04◇	-5.43	26.93	0.13	26.61	0.32
-93.14◇	-4.96	26.63	0.10	26.56	0.32
-84.68◇	-4.51	26.31	0.09	26.13	0.24
-76.56◇	-4.07	26.08	0.08	25.86	0.20
-64.93◇	-3.46	25.84	0.07	25.30	0.13
-61.08◇	-3.25	25.54	0.06	25.14	0.12
-49.97◇	-2.66	24.94	0.03	24.45	0.07
-48.09◇	-2.56	24.66	0.03	24.29	0.06
-44.49◇	-2.37	24.45	0.02	24.02	0.05
-42.70◇	-2.27	24.17	0.02	23.84	0.04
-34.01◇	-1.81	···	···	23.00	0.02
-27.17◇	-1.45	···	···	22.30	0.01
-22.04•	-1.17	···	···	21.68	0.01
-18.62•	-0.99	···	···	21.38	0.02
25.84•	1.38	···	···	22.04	0.02
32.68•	1.74	···	···	22.68	0.01
39.52•	2.10	···	···	23.36	0.02
46.36•	2.47	···	···	24.11	0.04
25.84•	1.38	···	···	22.04	0.02
32.68•	1.74	···	···	22.68	0.01
39.52•	2.10	···	···	23.36	0.02
46.36•	2.47	···	···	24.11	0.04
53.49•	2.85	25.22	0.04	24.72	0.07
57.17•	3.04	25.45	0.04	24.94	0.08
70.33•	3.74	26.01	0.06	25.55	0.14
80.08•	4.26	26.29	0.08	25.90	0.19
88.20•	4.69	26.41	0.09	26.23	0.25
96.67•	5.14	26.78	0.12	26.49	0.30
105.56•	5.62	26.89	0.13	27.02	0.47
115.05•	6.12	27.12	0.15	27.27	0.58
120.01•	6.39	27.18	0.16	27.92	1.04
125.14•	6.66	27.33	0.18	···	···
130.52•	6.95	27.40	0.19	···	···

TABLE 5. (continued)

distance (arcsec)	distance (kpc)	6660Å (mag/sq arcsec)	error(6660Å) (mag/sq arcsec)	8020Å (mag/sq arcsec)	error(8020Å) (mag/sq arcsec)
136.17•	7.25	27.47	0.20	···	···
142.07•	7.56	27.64	0.23	···	···
148.22•	7.89	27.74	0.25	···	···
154.81•	8.24	28.03	0.33	···	···
161.73•	8.61	28.23	0.39	···	···
169.08•	9.00	28.51	0.51	···	···
176.95•	9.42	28.65	0.57	27.74	0.81
186.44•	9.92	28.75	0.63	27.74	0.81
196.84•	10.48	29.15	0.91	27.88	0.92
207.10•	11.02	···	···	27.90	0.94
217.36•	11.57	···	···	27.88	0.93
225.91•	12.02	···	···	27.58	0.71
233.60•	12.43	···	···	27.71	0.80
239.59•	12.75	···	···	27.74	0.83
Cut B1, $r = 4.1$ kpc					
-178.68•	-9.51	28.92	0.73	···	···
-171.75•	-9.14	28.85	0.68	···	···
-163.89•	-8.72	28.73	0.62	27.74	0.83
-156.53•	-8.33	28.71	0.61	27.39	0.60
-149.61•	-7.96	28.53	0.52	27.16	0.50
-143.02•	-7.61	28.33	0.44	27.00	0.43
-136.87•	-7.28	28.17	0.38	27.13	0.49
-130.97•	-6.97	28.06	0.35	27.04	0.45
-125.33•	-6.67	27.99	0.33	27.01	0.45
-119.94•	-6.38	27.69	0.25	26.92	0.41
-114.81◇	-6.11	27.58	0.23	26.87	0.40
-107.37◇	-5.71	27.28	0.18	26.83	0.41
-100.36◇	-5.34	27.06	0.16	26.55	0.33
-95.91◇	-5.10	26.94	0.14	26.66	0.39
-89.33◇	-4.75	26.87	0.14	26.15	0.25
-83.00◇	-4.42	26.71	0.12	26.01	0.21
-78.98◇	-4.20	26.52	0.10	25.80	0.18
-72.91◇	-3.88	26.36	0.09	25.92	0.21
-68.98◇	-3.67	26.16	0.07	25.67	0.18
-65.13◇	-3.47	26.00	0.06	25.66	0.17
-61.29◇	-3.26	25.84	0.05	25.25	0.12
-57.52◇	-3.06	25.61	0.04	24.93	0.08
-53.85◇	-2.87	25.34	0.03	24.79	0.07
-46.41◇	-2.47	24.79	0.02	24.38	0.05
-42.82◇	-2.28	24.43	0.02	23.97	0.03
-39.31◇	-2.09	24.02	0.01	23.70	0.03
-35.89◇	-1.91	23.75	0.01	23.31	0.02
-32.47◇	-1.73	23.44	0.01	22.97	0.02
-27.34◇	-1.46	23.12	0.02	22.52	0.01
-20.26◇	-1.08	···	···	21.68	0.01
24.20•	1.29	···	···	22.07	0.01

TABLE 5. (continued)

distance (arcsec)	distance (kpc)	6660Å (mag/sq arcsec)	error(6660Å) (mag/sq arcsec)	8020Å (mag/sq arcsec)	error(8020Å) (mag/sq arcsec)
30.80•	1.64	23.28	0.02	22.74	0.01
34.22•	1.82	23.52	0.01	23.30	0.02
37.64•	2.00	23.97	0.01	23.62	0.03
41.06•	2.18	24.25	0.02	23.93	0.04
44.48•	2.37	24.53	0.02	24.29	0.05
49.69•	2.64	24.95	0.03	24.65	0.07
53.28•	2.84	25.13	0.03	24.92	0.08
56.96•	3.03	25.50	0.04	25.20	0.11
62.52•	3.33	25.82	0.05	25.34	0.12
68.16•	3.63	26.08	0.07	25.51	0.14
72.01•	3.83	26.21	0.07	25.57	0.14
75.86•	4.04	26.24	0.07	25.67	0.15
79.79•	4.25	26.24	0.07	25.90	0.18
83.81•	4.46	26.46	0.09	26.28	0.26
87.83•	4.67	26.59	0.10	26.30	0.26
92.02•	4.90	26.60	0.10	26.33	0.27
98.34•	5.23	26.68	0.11	26.49	0.30
105.01•	5.59	26.82	0.12	26.84	0.42
109.54•	5.83	26.87	0.13	27.12	0.54
114.25•	6.08	26.85	0.12	27.51	0.81
119.12•	6.34	27.04	0.15	···	···
124.25•	6.61	27.15	0.16	···	···
129.46•	6.89	27.27	0.18	···	···
134.94•	7.18	27.31	0.19	···	···
140.75•	7.49	27.31	0.18	27.76	0.90
146.74•	7.81	27.42	0.20	27.84	0.95
153.15•	8.15	27.60	0.23	27.91	1.00
159.90•	8.51	27.66	0.24	27.83	0.93
167.00•	8.89	27.73	0.26	27.77	0.87
174.61•	9.29	27.79	0.28	27.64	0.75
180.42•	9.60	27.84	0.29	27.51	0.67
188.12•	10.01	27.83	0.29	27.54	0.69
194.96•	10.37	27.88	0.30	27.79	0.86
201.80•	10.74	27.89	0.31	27.75	0.84
208.64•	11.10	27.88	0.31	27.84	0.91
215.48•	11.47	27.86	0.31	27.90	0.96
220.61•	11.74	27.88	0.32	27.95	1.01
227.45•	12.10	27.78	0.29	27.78	0.86
235.14•	12.51	27.81	0.31	27.57	0.71
242.84•	12.92	28.26	0.47	27.61	0.74
249.68•	13.29	28.31	0.47	27.63	0.74
256.52•	13.65	28.51	0.55	27.77	0.84
264.21•	14.06	28.78	0.68	···	···
272.76•	14.52	28.47	0.50	···	···
Cut B2, $r = -4.1$ kpc					
-271.62•	-14.45	28.60	0.54	···	···
-268.20•	-14.27	28.58	0.53	···	···

TABLE 5. (continued)

distance (arcsec)	distance (kpc)	6660Å (mag/sq arcsec)	error(6660Å) (mag/sq arcsec)	8020Å (mag/sq arcsec)	error(8020Å) (mag/sq arcsec)
-263.07•	-14.00	28.52	0.50	···	···
-257.94•	-13.73	28.55	0.51	···	···
-251.95•	-13.41	28.44	0.46	···	···
-246.82•	-13.13	28.38	0.44	···	···
-243.40•	-12.95	28.27	0.40	···	···
-238.27•	-12.68	28.21	0.38	···	···
-232.29•	-12.36	28.13	0.35	···	···
-227.16•	-12.09	28.06	0.33	···	···
-221.17•	-11.77	28.08	0.33	···	···
-216.04•	-11.50	28.07	0.33	···	···
-210.91•	-11.22	28.07	0.33	···	···
-207.49•	-11.04	28.00	0.31	···	···
-202.36•	-10.77	27.94	0.30	27.94	0.98
-197.23•	-10.50	27.88	0.28	···	···
-192.19•	-10.23	27.86	0.28	27.72	0.80
-186.97•	-9.95	27.87	0.28	27.68	0.78
-180.99•	-9.63	27.86	0.28	27.70	0.79
-174.06•	-9.26	27.84	0.28	27.72	0.81
-166.19•	-8.84	27.84	0.28	27.62	0.75
-158.84•	-8.45	27.72	0.26	27.49	0.68
-151.92•	-8.08	27.75	0.27	27.60	0.77
-145.33•	-7.73	27.75	0.28	27.54	0.74
-139.18•	-7.41	27.55	0.24	27.23	0.58
-133.28•	-7.09	27.47	0.22	27.20	0.57
-127.63•	-6.79	27.45	0.22	27.29	0.63
-122.25•	-6.51	27.32	0.20	27.10	0.53
-117.12◇	-6.23	27.26	0.19	26.61	0.35
-107.37◇	-5.71	27.05	0.15	26.74	0.38
-100.45◇	-5.35	26.99	0.14	26.67	0.36
-91.64◇	-4.88	26.75	0.11	26.28	0.25
-85.31◇	-4.54	26.58	0.10	26.04	0.21
-79.24◇	-4.22	26.40	0.09	25.97	0.20
-73.26◇	-3.90	26.25	0.08	26.07	0.22
-67.44◇	-3.59	26.04	0.06	25.81	0.17
-61.71◇	-3.28	25.90	0.06	25.49	0.13
-57.95◇	-3.08	25.65	0.05	25.30	0.11
-54.28◇	-2.89	25.39	0.04	25.08	0.09
-50.60◇	-2.69	25.11	0.03	25.02	0.09
-46.92◇	-2.50	24.88	0.02	24.56	0.06
-43.33◇	-2.31	24.50	0.02	24.34	0.05
-39.91◇	-2.12	24.12	0.01	24.02	0.04
-36.49◇	-1.94	23.79	0.01	23.65	0.03
-33.07◇	-1.76	23.45	0.01	23.20	0.02
-29.65◇	-1.58	23.14	0.01	22.75	0.01
-26.23◇	-1.40	22.83	0.01	22.29	0.01
-17.68◇	-0.94	···	···	21.43	0.01
-15.97◇	-0.85	···	···	21.42	0.01

TABLE 5. (continued)

distance (arcsec)	distance (kpc)	6660Å (mag/sq arcsec)	error(6660Å) (mag/sq arcsec)	8020Å (mag/sq arcsec)	error(8020Å) (mag/sq arcsec)
25.07•	1.33	···	···	22.52	0.02
35.33•	1.88	23.72	0.01	23.34	0.03
38.75•	2.06	23.99	0.01	23.68	0.04
42.17•	2.24	24.36	0.02	24.26	0.06
45.59•	2.43	24.69	0.02	24.31	0.06
49.18•	2.62	24.99	0.03	24.63	0.08
52.86•	2.81	25.32	0.04	24.92	0.10
58.41•	3.11	25.66	0.05	25.26	0.12
62.09•	3.30	25.79	0.05	25.39	0.14
65.85•	3.50	25.97	0.06	25.86	0.21
69.70•	3.71	26.15	0.07	25.69	0.17
75.51•	4.02	26.32	0.08	26.20	0.27
81.50•	4.34	26.47	0.09	26.57	0.36
87.57•	4.66	26.59	0.10	27.18	0.61
91.76•	4.88	26.75	0.11	27.48	0.78
96.03•	5.11	26.87	0.13	27.26	0.63
102.70•	5.47	27.05	0.15	27.15	0.58
109.63•	5.83	27.20	0.17	26.96	0.47
114.42•	6.09	27.45	0.20	27.59	0.82
119.38•	6.35	27.59	0.23	27.56	0.78
124.51•	6.63	27.59	0.23	27.41	0.67
129.89•	6.91	27.66	0.24	···	···
135.53•	7.21	27.69	0.25	···	···
141.43•	7.53	27.81	0.27	27.59	0.76
147.59•	7.85	27.98	0.32	27.55	0.73
154.17•	8.20	28.03	0.33	27.53	0.70
161.10•	8.57	28.21	0.38	27.76	0.86
168.45•	8.96	28.40	0.46	27.69	0.79
176.32•	9.38	28.59	0.54	27.72	0.81
183.24•	9.75	28.80	0.65	27.78	0.86
189.23•	10.07	29.11	0.87	27.58	0.71
Cut C1, $r = 8.2$ kpc					
-146.38•	-7.79	28.90	0.74	···	···
-136.97•	-7.29	28.84	0.72	···	···
-128.16•	-6.82	28.81	0.72	···	···
-120.04•	-6.39	28.34	0.49	···	···
-112.35•	-5.98	28.24	0.46	···	···
-105.17•	-5.60	28.03	0.38	···	···
-98.24•	-5.23	27.51	0.23	···	···
-91.57◇	-4.87	27.32	0.19	27.33	0.70
-85.24◇	-4.54	27.02	0.15	26.73	0.41
-79.09◇	-4.21	27.00	0.15	26.98	0.53
-73.02◇	-3.89	26.82	0.13	26.87	0.49
-69.08◇	-3.68	26.49	0.10	26.12	0.24
-65.24◇	-3.47	26.31	0.08	26.21	0.26
-61.39◇	-3.27	26.06	0.07	26.05	0.23
-57.63◇	-3.07	25.81	0.05	25.49	0.14

TABLE 5. (continued)

distance (arcsec)	distance (kpc)	6660Å (mag/sq arcsec)	error(6660Å) (mag/sq arcsec)	8020Å (mag/sq arcsec)	error(8020Å) (mag/sq arcsec)
-52.07◇	-2.77	25.50	0.04	25.16	0.11
-48.39◇	-2.58	25.16	0.03	24.77	0.08
-44.72◇	-2.38	24.80	0.02	24.43	0.06
-41.13◇	-2.19	24.55	0.02	24.23	0.05
-39.42◇	-2.10	24.30	0.01	24.11	0.05
-36.00◇	-1.92	24.07	0.01	23.69	0.03
-32.58◇	-1.73	23.77	0.01	23.41	0.02
-29.16◇	-1.55	23.41	0.01	23.09	0.02
-17.19◇	-0.91	22.33	0.01	21.90	0.01
-14.71◇	-0.78	···	···	21.67	0.01
23.85◇	1.27	22.71	0.01	22.27	0.01
25.56◇	1.36	22.92	0.01	22.52	0.01
27.27◇	1.45	23.10	0.01	22.70	0.01
32.40◇	1.72	23.56	0.01	23.32	0.02
35.82◇	1.91	23.97	0.01	23.77	0.03
37.53◇	2.00	24.15	0.01	24.06	0.04
39.24◇	2.09	24.39	0.02	24.28	0.05
42.66◇	2.27	24.70	0.02	24.48	0.06
46.08◇	2.45	24.97	0.03	24.71	0.07
51.39◇	2.73	25.42	0.04	25.07	0.10
55.06◇	2.93	25.81	0.06	25.45	0.14
58.74◇	3.13	25.86	0.06	26.09	0.26
64.30◇	3.42	26.19	0.08	26.00	0.24
70.02◇	3.73	26.36	0.09	25.77	0.18
75.75◇	4.03	26.50	0.10	26.58	0.37
81.65◇	4.35	26.66	0.11	26.62	0.35
87.72◇	4.67	26.73	0.11	26.50	0.31
93.96◇	5.00	26.89	0.13	26.49	0.30
100.46◇	5.35	27.05	0.16	26.85	0.42
107.13◇	5.70	27.29	0.20	27.44	0.73
114.14◇	6.07	27.29	0.20	27.22	0.60
121.58◇	6.47	27.33	0.21	27.08	0.54
129.36◇	6.88	27.35	0.21	26.96	0.48
137.74◇	7.33	27.33	0.21	26.74	0.39
146.63◇	7.80	27.29	0.20	26.43	0.28
156.38◇	8.32	27.33	0.22	26.25	0.24
163.31◇	8.69	27.40	0.23	26.26	0.24
170.66◇	9.08	27.42	0.24	26.29	0.25
180.32◇	9.60	27.49	0.27	26.29	0.25
188.01◇	10.01	27.78	0.34	26.61	0.33
194.85◇	10.37	27.86	0.36	26.93	0.43
201.69◇	10.73	27.75	0.32	27.27	0.58
208.53◇	11.10	27.95	0.35	27.38	0.63
215.37◇	11.46	28.08	0.38	···	···
222.21◇	11.83	28.11	0.37	···	···
229.91◇	12.23	28.00	0.33	···	···
236.75◇	12.60	27.96	0.32	···	···

TABLE 5. (continued)

distance (arcsec)	distance (kpc)	6660Å (mag/sq arcsec)	error(6660Å) (mag/sq arcsec)	8020Å (mag/sq arcsec)	error(8020Å) (mag/sq arcsec)
242.73◇	12.92	27.98	0.32	···	···
249.57◇	13.28	27.99	0.32	···	···
256.41◇	13.65	28.02	0.33	27.97	1.01
262.40◇	13.96	28.02	0.32	···	···
269.24◇	14.33	28.02	0.32	27.93	0.97
276.08◇	14.69	28.03	0.32	···	···
Cut C2, $r = -8.2$ kpc					
-188.78	-10.05	28.81	0.66	···	···
-180.23	-9.59	28.80	0.66	27.57	0.70
-171.85	-9.15	28.63	0.57	27.49	0.66
-164.25	-8.74	28.34	0.44	27.53	0.69
-153.73	-8.18	28.23	0.40	27.47	0.66
-143.98	-7.66	27.96	0.32	27.24	0.55
-135.09	-7.19	27.67	0.25	26.92	0.43
-126.71	-6.74	27.44	0.20	26.63	0.33
-118.93◇	-6.33	27.36	0.19	26.57	0.33
-111.49◇	-5.93	27.13	0.16	26.43	0.30
-104.48◇	-5.56	27.10	0.15	26.87	0.47
-97.81◇	-5.21	26.89	0.13	26.67	0.41
-91.31◇	-4.86	26.65	0.11	26.91	0.52
-85.07◇	-4.53	26.53	0.10	26.12	0.27
-79.00◇	-4.20	26.49	0.10	26.92	0.57
-73.10◇	-3.89	26.48	0.10	26.33	0.30
-69.26◇	-3.69	26.15	0.07	25.92	0.20
-65.41◇	-3.48	25.94	0.06	25.82	0.19
-61.65◇	-3.28	25.79	0.05	25.75	0.19
-56.09◇	-2.98	25.72	0.05	25.42	0.14
-50.53◇	-2.69	25.47	0.04	25.30	0.13
-45.14◇	-2.40	25.09	0.03	25.07	0.10
-40.01◇	-2.13	24.61	0.02	24.41	0.06
-34.88◇	-1.86	24.12	0.01	24.07	0.04
-31.46◇	-1.67	23.66	0.01	23.59	0.03
-28.04◇	-1.49	23.42	0.01	23.26	0.02
-26.33◇	-1.40	23.22	0.01	22.99	0.02
-22.91◇	-1.22	23.09	0.02	22.62	0.01
-19.12◇	-1.02	···	···	21.99	0.03
15.08◇	0.80	···	···	21.71	0.01
21.55◇	1.15	23.03	0.02	22.56	0.01
23.26◇	1.24	23.21	0.01	22.69	0.01
26.68◇	1.42	23.56	0.01	23.00	0.01
28.39◇	1.51	23.57	0.01	23.17	0.02
31.81◇	1.69	23.87	0.01	23.55	0.02
36.94◇	1.97	24.33	0.01	24.02	0.04
43.78◇	2.33	24.95	0.03	24.64	0.07
49.16◇	2.62	25.37	0.04	25.17	0.10
54.72◇	2.91	25.79	0.05	25.63	0.16

TABLE 5. (continued)

distance (arcsec)	distance (kpc)	6660Å (mag/sq arcsec)	error(6660Å) (mag/sq arcsec)	8020Å (mag/sq arcsec)	error(8020Å) (mag/sq arcsec)
58.40◇	3.11	25.98	0.06	25.65	0.16
64.04◇	3.41	26.17	0.08	25.92	0.21
71.73◇	3.82	26.33	0.09	26.19	0.27
75.67◇	4.03	26.51	0.10	26.51	0.37
81.74◇	4.35	26.69	0.11	27.44	0.81
87.89◇	4.68	26.73	0.11	27.47	0.82
94.22◇	5.01	27.01	0.14	27.64	0.91
100.89◇	5.37	27.32	0.19	···	···
107.82◇	5.74	27.57	0.23	···	···
115.00◇	6.12	27.64	0.24	···	···
122.69◇	6.53	27.68	0.25	27.54	0.75
130.81◇	6.96	27.68	0.24	27.25	0.57
139.62◇	7.43	27.64	0.23	27.40	0.65
149.03◇	7.93	27.80	0.27	27.55	0.73
159.29	8.48	27.95	0.30	···	···
166.64	8.87	28.04	0.33	···	···
176.30	9.38	28.14	0.36	27.77	0.86
185.71	9.88	28.19	0.37	27.77	0.86
192.63	10.25	28.25	0.40	27.94	1.01
199.39	10.61	28.25	0.40	27.85	0.93
206.23	10.97	28.34	0.43	27.85	0.93
213.07	11.34	28.52	0.51	27.88	0.95
219.91	11.70	28.64	0.57	···	···
227.60	12.11	28.71	0.60	···	···
234.44	12.48	28.76	0.63	···	···
242.14	12.89	28.93	0.74	27.73	0.81
249.35	13.27	29.02	0.80	27.65	0.76
Cut D1, $r = 12.3$ kpc					
-105.59	-5.62	28.58	0.58	···	···
-98.41	-5.24	28.51	0.55	···	···
-91.66	-4.88	28.38	0.50	···	···
-85.07	-4.53	27.90	0.33	···	···
-78.75	-4.19	27.69	0.27	···	···
-72.67	-3.87	27.67	0.27	···	···
-66.69	-3.55	27.29	0.20	27.49	0.85
-62.84	-3.34	26.82	0.13	26.97	0.53
-57.03	-3.03	26.55	0.11	27.33	0.80
-51.39	-2.73	26.15	0.08	25.79	0.19
-45.83	-2.44	25.70	0.05	25.44	0.13
-40.36	-2.15	25.25	0.03	25.00	0.10
-33.34	-1.77	24.74	0.02	24.33	0.06
-28.22	-1.50	24.31	0.02	23.99	0.04
-26.50	-1.41	24.01	0.01	23.85	0.04
-24.79	-1.32	24.05	0.01	23.65	0.03
-23.09	-1.23	23.85	0.01	23.62	0.03
-21.38	-1.14	23.78	0.01	23.63	0.03
-19.66	-1.05	23.62	0.01	23.70	0.03

TABLE 5. (continued)

distance (arcsec)	distance (kpc)	6660Å (mag/sq arcsec)	error(6660Å) (mag/sq arcsec)	8020Å (mag/sq arcsec)	error(8020Å) (mag/sq arcsec)
-15.34	-0.82	23.50	0.01	22.26	0.01
20.57◇	1.09	22.84	0.01	22.56	0.01
23.99◇	1.28	23.29	0.01	23.02	0.02
26.50◇	1.41	23.85	0.01	23.76	0.03
28.22◇	1.50	24.10	0.01	24.03	0.04
33.34◇	1.77	24.47	0.02	24.49	0.06
36.76◇	1.96	24.94	0.03	24.70	0.08
41.89◇	2.23	25.59	0.05	25.39	0.15
48.73◇	2.59	26.03	0.08	25.68	0.19
52.16◇	2.78	26.30	0.10	25.75	0.21
57.54◇	3.06	26.80	0.16	26.34	0.36
64.98◇	3.46	26.75	0.14	27.28	0.79
70.54◇	3.75	26.82	0.15	26.80	0.49
74.39◇	3.96	27.22	0.20	27.06	0.57
80.11◇	4.26	27.21	0.19	26.78	0.43
86.01◇	4.58	27.07	0.16	26.76	0.42
92.08◇	4.90	27.20	0.18	27.28	0.67
98.33◇	5.23	27.35	0.20	···	···
102.60◇	5.46	27.53	0.23	···	···
109.27◇	5.81	27.55	0.23	···	···
116.19◇	6.18	27.56	0.23	···	···
123.38◇	6.57	27.78	0.28	···	···
131.07◇	6.98	27.97	0.32	···	···
139.19◇	7.41	27.99	0.33	27.85	0.97
148.00◇	7.88	27.99	0.32	27.93	1.02
157.41◇	8.38	28.02	0.33	···	···
167.67◇	8.92	28.04	0.33	27.73	0.83
178.87◇	9.52	28.05	0.33	27.48	0.65
189.81◇	10.10	28.11	0.35	27.42	0.61
199.22◇	10.60	28.17	0.37	27.36	0.58
207.76◇	11.06	28.21	0.38	27.59	0.71
216.31◇	11.51	28.30	0.41	27.67	0.76
226.57◇	12.06	28.32	0.42	27.66	0.76
235.98◇	12.56	28.40	0.45	27.71	0.79
245.39◇	13.06	28.45	0.48	27.75	0.82
253.93◇	13.51	28.49	0.50	27.67	0.76
263.34◇	14.01	28.55	0.53	27.68	0.77
271.89◇	14.47	28.62	0.58	···	···
280.44◇	14.92	28.64	0.60	···	···
Cut D2, $r = -12.3$ kpc					
-272.23	-14.49	···	···	28.16	1.18
-261.97	-13.94	···	···	28.31	1.36
-250.86	-13.35	···	···	28.08	1.10
-240.60	-12.80	···	···	28.09	1.10
-229.48	-12.21	···	···	28.03	1.05
-220.08	-11.71	···	···	28.21	1.25

TABLE 5. (continued)

distance (arcsec)	distance (kpc)	6660Å (mag/sq arcsec)	error(6660Å) (mag/sq arcsec)	8020Å (mag/sq arcsec)	error(8020Å) (mag/sq arcsec)
-209.82	-11.17	···	···	27.84	0.89
-197.85	-10.53	···	···	27.60	0.73
-185.88	-9.89	···	···	27.61	0.74
-176.16	-9.37	27.96	0.38	27.14	0.49
-164.54	-8.76	28.47	0.64	26.93	0.41
-154.02	-8.20	28.54	0.68	26.97	0.45
-144.27	-7.68	28.48	0.63	27.18	0.55
-135.38	-7.20	28.56	0.67	27.42	0.68
-127.00	-6.76	27.97	0.39	27.56	0.78
-119.22	-6.34	27.80	0.33	···	···
-114.26	-6.08	27.52	0.25	···	···
-109.47	-5.83	27.33	0.21	···	···
-104.77	-5.58	27.63	0.28	27.09	0.53
-98.10	-5.22	27.65	0.27	27.12	0.56
-91.60	-4.87	27.52	0.24	27.20	0.60
-85.36	-4.54	27.23	0.18	···	···
-79.29	-4.22	27.13	0.17	26.93	0.48
-73.39	-3.91	27.09	0.16	26.70	0.41
-67.66	-3.60	26.94	0.15	26.54	0.36
-61.94	-3.30	26.62	0.11	26.16	0.26
-56.38	-3.00	26.42	0.10	26.07	0.24
-49.03	-2.61	26.07	0.07	26.05	0.24
-43.72	-2.33	25.54	0.05	25.43	0.14
-40.30	-2.14	25.13	0.03	24.92	0.09
-35.17	-1.87	24.59	0.02	24.63	0.07
-31.75	-1.69	24.17	0.01	24.03	0.04
-28.33	-1.51	23.89	0.01	23.71	0.03
-26.62	-1.42	23.68	0.01	23.51	0.03
-23.20	-1.23	23.56	0.01	23.25	0.02
-12.09	-0.64	22.79	0.01	23.02	0.02
-6.96	-0.37	22.45	0.01	22.83	0.02
-5.25	-0.28	22.45	0.01	22.60	0.02
1.59◇	0.08	22.22	0.01	22.49	0.01
8.43◇	0.45	22.60	0.01	22.80	0.02
12.71◇	0.68	22.90	0.01	23.08	0.02
16.13◇	0.86	23.18	0.01	23.22	0.02
22.97◇	1.22	23.46	0.01	23.73	0.03
28.10◇	1.50	23.89	0.01	23.85	0.03
29.81◇	1.59	24.02	0.01	24.08	0.04
31.52◇	1.68	24.32	0.01	24.32	0.05
36.65◇	1.95	24.92	0.02	24.73	0.08
40.07◇	2.13	25.32	0.04	24.88	0.09
47.08◇	2.51	25.81	0.06	25.48	0.15
50.75◇	2.70	26.14	0.08	25.46	0.14
58.11◇	3.09	26.26	0.08	26.18	0.28
65.72◇	3.50	26.34	0.09	26.08	0.24
71.44◇	3.80	26.62	0.11	26.20	0.26

TABLE 5. (continued)

distance (arcsec)	distance (kpc)	6660Å (mag/sq arcsec)	error(6660Å) (mag/sq arcsec)	8020Å (mag/sq arcsec)	error(8020Å) (mag/sq arcsec)
77.34◇	4.12	26.77	0.13	26.60	0.39
83.41◇	4.44	26.70	0.12	27.35	0.78
87.60◇	4.66	27.02	0.17	···	···
93.93◇	5.00	27.21	0.19	···	···
100.60◇	5.35	27.12	0.17	···	···
107.52◇	5.72	27.26	0.18	27.76	0.98
114.71◇	6.10	27.35	0.19	27.73	0.97
122.40◇	6.51	27.41	0.20	···	···
130.52◇	6.95	27.35	0.18	27.67	0.84
139.33◇	7.41	27.40	0.19	27.68	0.92
148.74◇	7.92	27.43	0.19	···	···
159.00◇	8.46	27.53	0.21	···	···
170.20◇	9.06	27.61	0.22	···	···
178.58◇	9.50	27.73	0.25	···	···
187.13◇	9.96	27.77	0.25	···	···
197.39◇	10.50	27.80	0.26	···	···
205.94◇	10.96	27.75	0.25	···	···
214.49◇	11.41	27.73	0.24	27.98	1.02
223.04◇	11.87	27.69	0.23	27.76	0.83
232.44◇	12.37	27.70	0.23	27.30	0.55
240.14◇	12.78	27.64	0.22	27.25	0.51
246.98◇	13.14	27.62	0.22	27.22	0.50
254.67◇	13.55	27.56	0.21	27.23	0.51
263.22◇	14.01	27.55	0.20	27.14	0.47
271.77◇	14.46	27.52	0.20	···	···

[a]The data marked with • are affected by foreground star contamination and a possible line-of-sight warp.

[b]The data marked with ◇ are affected by the ring.

TABLE 6. Morrison et al. surface brightness profiles of NGC 5907 in R band

distance (arcsec)	distance (kpc)	R (mag/sq arcsec)	high error (mag/sq arcsec)	low error (mag/sq arcsec)
Cut A, $r = 0$ kpc				
11.55	0.61	19.99	0.00	0.00
15.79	0.84	20.51	0.00	0.00
19.69	1.05	21.08	0.00	0.00
23.81	1.27	21.69	0.00	0.00
27.00	1.44	22.13	0.00	0.00
30.82	1.64	22.62	0.01	0.01
34.65	1.84	23.09	0.01	0.01
38.46	2.05	23.53	0.01	0.01
42.25	2.25	23.95	0.02	0.02
46.19	2.46	24.35	0.03	0.03
50.02	2.66	24.69	0.04	0.04
53.90	2.87	24.98	0.05	0.06
57.76	3.08	25.20	0.06	0.07
62.30	3.32	25.50	0.11	0.13
67.73	3.61	25.74	0.14	0.16
74.04	3.94	25.76	0.10	0.11
82.59	4.40	25.92	0.11	0.13
94.78	5.05	26.37	0.17	0.20
123.88	6.60	26.95	0.27	0.36
183.67	9.78	27.20	0.33	0.47
260.55	13.87	27.84	0.53	1.10
334.53	17.81	28.00	0.60	1.44
410.94	21.88	28.28	0.73	3.36
466.15	24.82	33.40	4.33	0.00
Cut B, $r = 4.1$ kpc				
5.78	0.31	19.92	0.00	0.00
8.23	0.44	20.11	0.00	0.00
12.19	0.65	20.65	0.00	0.00
15.97	0.85	21.05	0.00	0.00
20.31	1.08	21.60	0.07	0.07
23.49	1.25	22.02	0.03	0.03
27.09	1.44	22.46	0.05	0.05
30.80	1.64	22.91	0.04	0.04
34.65	1.84	23.36	0.06	0.06
38.51	2.05	23.79	0.11	0.12
42.38	2.26	24.20	0.12	0.14
46.17	2.46	24.60	0.13	0.14
50.05	2.67	24.87	0.14	0.16
53.94	2.87	25.21	0.14	0.16
57.74	3.07	25.43	0.18	0.21
62.26	3.32	25.69	0.21	0.26
67.82	3.61	25.98	0.17	0.20
73.92	3.94	26.17	0.19	0.24
82.27	4.38	26.30	0.27	0.35
94.99	5.06	26.54	0.37	0.56
125.02	6.66	27.01	0.46	0.83

TABLE 6. (continued)

distance (arcsec)	distance (kpc)	R (mag/sq arcsec)	high error (mag/sq arcsec)	low error (mag/sq arcsec)
183.68	9.78	27.43	0.42	0.70
262.36	13.97	27.96	0.72	3.17
333.43	17.75	27.88	0.59	1.37
415.87	22.14	28.57	0.73	3.30
466.49	24.84	33.40	5.15	0.00
Cut C, $r = 8.2$ kpc				
20.82	1.11	21.84	0.01	0.01
23.55	1.25	22.42	0.19	0.23
26.97	1.44	22.88	0.14	0.17
30.81	1.64	23.35	0.11	0.12
34.66	1.85	23.81	0.07	0.08
38.55	2.05	24.23	0.08	0.09
42.34	2.25	24.58	0.12	0.13
46.21	2.46	24.92	0.15	0.17
50.04	2.66	25.17	0.13	0.15
53.92	2.87	25.47	0.13	0.15
57.74	3.07	25.62	0.16	0.19
62.32	3.32	25.85	0.15	0.17
67.74	3.61	26.02	0.09	0.10
73.93	3.94	26.17	0.10	0.12
82.39	4.39	26.36	0.15	0.18
94.98	5.06	26.61	0.22	0.27
123.47	6.57	26.83	0.18	0.21
184.48	9.82	27.24	0.53	1.07
261.75	13.94	28.40	1.05	5.00
331.70	17.66	27.92	0.78	5.48
413.16	22.00	27.96	0.78	5.44
462.21	24.61	28.05	0.66	1.98
Cut D, $r = 12.3$ kpc				
16.56	0.88	22.34	0.11	0.12
19.49	1.04	22.70	0.17	0.21
23.33	1.24	23.16	0.09	0.10
26.98	1.44	23.62	0.07	0.07
30.84	1.64	23.98	0.06	0.06
34.63	1.84	24.39	0.03	0.03
38.54	2.05	24.73	0.09	0.10
42.38	2.26	25.09	0.08	0.08
46.24	2.46	25.40	0.12	0.14
49.95	2.66	25.69	0.09	0.09
53.92	2.87	25.88	0.21	0.25
57.74	3.07	26.04	0.25	0.33
62.52	3.33	26.19	0.20	0.24
67.78	3.61	26.33	0.25	0.32
73.85	3.93	26.39	0.34	0.49
82.73	4.41	26.68	0.34	0.51
94.64	5.04	26.93	0.34	0.49

TABLE 6. (continued)

distance (arcsec)	distance (kpc)	R (mag/sq arcsec)	high error (mag/sq arcsec)	low error (mag/sq arcsec)
124.14	6.61	27.28	0.57	1.25
185.07	9.85	27.51	0.69	2.31
259.71	13.83	27.93	0.87	5.47
337.33	17.96	27.75	0.89	5.65
403.18	21.47	27.80	0.87	5.60
469.57	25.00	28.40	0.96	5.00

TABLE 7. Comparisons to surface brightness profiles from other observers

Position	6660Å	8020Å	J	K_s	R	V	I
-145 to -120	27.80	27.22	25.64	24.48	-	-	-
-120 to -100	27.15	26.58	25.07	23.68	26.72	-	-
-100 to -80	26.64	26.35	24.59	23.25	26.31	27.58	26.36
-80 to -70	26.28	26.00	24.32	23.02	25.96	27.00	25.67
-70 to -60	25.82	25.53	24.16	22.85	25.71	26.50	25.29
-60 to -50	25.31	24.78	23.64	22.80	25.02	25.95	24.87
-50 to -40	24.58	24.17	22.80	22.04	24.15	25.04	24.09
-40 to -30	24.09	23.20	21.50	20.82	23.04	23.85	22.86
-30 to -20	-	22.40	20.05	19.34	21.79	22.63	21.59
-20 to -10	-	21.47	18.63	17.62	20.56	21.65	20.45
0							
10 to 20	-	-	18.74	17.71	20.56	20.92	19.62
20 to 30	-	22.37	20.40	19.40	21.79	22.41	21.10
30 to 40	-	23.18	21.63	20.68	23.04	23.77	22.79
40 to 50	24.71	24.11	22.48	21.84	24.15	25.06	24.15
50 to 60	25.52	24.75	23.11	22.31	25.02	26.04	25.05
60 to 70	25.91	25.24	23.32	22.74	25.71	26.68	25.60
70 to 80	26.19	25.59	23.39	22.95	25.96	27.15	25.99
80 to 100	26.61	26.57	23.76	23.13	26.31	27.67	26.52
100 to 120	27.06	27.23	24.10	22.69	26.72	28.30	27.08
120 to 145	27.60	-	25.38	24.88	-	-	27.08